Parametric Assessment of Wind Farm Performance Under Varying Terrain and Atmospheric Stability Using an Analytical Wake Model

First Author[a,*], Second Author[a]

[a]Department of Engineering Science, University of Oxford, Oxford, OX1 3PJ, United Kingdom

Abstract

Stability-driven differences in wind farm power output are commonly attributed to stability-dependent wake recovery rates, but the relative contributions of hub-height wind speed and wake dynamics to the total power variation are rarely separated. This paper presents a matched-velocity sensitivity demonstrating that when hub-height wind speed is held constant at 9.0 m s^{-1} across stable, neutral, and convective conditions, the combined stability effect on wake recovery accounts for only approximately 7% variation in farm power. By contrast, the total power variation across stability classes exceeds a factor of 2.3 when each condition is assigned its Weibull-distribution-mean reference (IEC 61400-1 power-class I wind speed: 7.1, 9.0, and 10.9 m s^{-1}), demonstrating that the dominant driver of stability-related power differences is the hub-height wind speed, not the wake expansion rate. These findings emerge from a systematic parametric assessment using the Bastankhah and Porté-Agel Gaussian wake model with stability-dependent and terrain-dependent wake expansion corrections, applied to a nine-turbine wind farm (3 000 D × 3 000 D layout) across three terrain types (flat, hilly, mountainous) and three stability conditions, producing a 3 × 3 parametric matrix. Terrain complexity exerts a secondary influence, with mountainous terrain producing 2.4% more power than flat terrain through enhanced wake mixing. The terrain–stability interaction is non-additive: terrain-enhanced mixing provides the greatest proportional benefit under stable conditions (+ 4%), and negligible benefit un-

*Corresponding author

Email address: first.author@eng.ox.ac.uk (First Author)

dry convective conditions ($z/L \approx 0.47$). Seasonal stratospheric variation produces a 46% swing in farm power, driven primarily by differences in prescribed friction velocity. Humidity corrections to air density reduce power estimates by up to 3.1% at high temperatures and humidities. The analytical predictions are compared against Reynolds-averaged Navier–Stokes (RANS) simulations performed in OpenFOAM for both a single actuator disk and the full 3×3 wind farm under neutral conditions; the single-turbine lateral wake profile RMSE decreases from 0.0309 at $x/D = 5$ to 0.0214 at $x/D = 10$, and the farm-level total power agrees to within 1.2%, while the Gaussian model consistently predicting deeper deficits than the RANS due to the known overprediction of turbulent mixing by the standard k–ε model. Under stable inflow conditions on the same flat mesh (7000 cells), the single-turbine RMSE ranges from 0.0261 at $x/D = 5$ to 0.0160 at $x/D = 10$, comparable to the neutral case. This comparison tests the wake model's response to a lower freestream velocity, using a neutral-shaped log-law inlet profile, but does not validate the stability correction factor or buoyancy-driven wake suppression, which would require a stability-corrected inlet and a thermally-coupled solver. The analytical framework enables rapid parametric exploration that can inform wind farm siting decisions, while its limitations relative to resolved computational fluid dynamics approaches are explicitly characterized.

Keywords: wind farm, analytical wake model, atmospheric stability, terrain effects, wake modelling, Gaussian wake, parametric study, Monin–Obukhov similarity, OpenFOAM, RANS validation

1. Introduction

Wind energy has experienced sustained global growth over the past two decades, with cumulative installed capacity exceeding 1,000 GW by the end of 2021 and ambitious national targets projecting a doubling of this capacity before 2030. As wind farms are increasingly deployed in locations with complex terrain and diverse climatic conditions, the accuracy of pre-construction energy yield assessments has become a critical factor in project financing and operational planning. Discrepancies between predicted and observed annual energy production (AEP) frequently exceed 10%, with a significant fraction of this uncertainty attributable to inadequate representation of local flow conditions arising from terrain, atmospheric interactions [1, 2].

Two broad classes of methods are available for predicting wind farm wake

losses. high-fidelity computational fluid dynamics (CFD) approaches, including Reynolds-averaged Navier–Stokes (RANS) modelling and large-eddy simulation (LES), and lower-order analytical engineering wake models [3, 4, 5]. LES provides the most detailed representation of wake physics, resolving turbulent structures that govern wake recovery and meandering [3, 4], but its computational cost restricts applications to a limited number of operating conditions. RANS models offer a middle ground, solving the mean-flow equations at lower cost, although the standard $k-\varepsilon$ turbulence model is known to overpredict wake recovery [5]. Analytical wake models, by contrast, provide results in seconds, enabling comprehensive parametric exploration across hundreds of conditions. The Gaussian wake model of Bastankhah and Porté-Agel [6], which assumes a self-similar Gaussian velocity deficit profile behind each turbine, has become one of the most widely adopted analytical models due to its physical basis and demonstrated accuracy for single-turbine wakes [6, 18]. Niayifar and Porté-Agel [12] extended this model to wind farm applications by incorporating a local turbulence intensity dependent wake expansion rate.

The influence of atmospheric stability on wind farm performance has received considerable attention in both observational and numerical studies. Field measurements by Wharton and Lundquist [13] demonstrated that individual turbine power output is strongly modulated by atmospheric stability through its effects on vertical wind shear and turbulence intensity. Hansen *et al.* [14] quantified stability-dependent power deficits at the Horns Rev offshore wind farm using SCADA data. LES studies by Abkar and Porté-Agel [14] and Lu and Porté-Agel [15] confirmed that convective conditions produce significantly faster wake dissipation than stable stratification. Du *et al.* [16] performed a controlled parametric study of atmospheric stability effects on wake recovery, strategically varying roughness and domain height to match turbulence intensity across stability classes, thereby isolating the stability effect from wind speed differences. Xie and Archer [17] investigated the self-similarity and turbulence characteristics of wind turbine wakes under different stability conditions using LES. Beck and Kleissl [18] systematically investigated the effects of wind shear, rotor turbulence intensity, Coriolis forcing, and thermal stratification on single-turbine wake dynamics using over 400 LES cases with a controlled synthetic inflow methodology. More recently, Yuan *et al.* [19] generated a comprehensive LES dataset spanning a complete diurnal cycle. Within the analytical modelling framework, Xiaris [20] proposed a stability-dependent correction to the Jensen wake model [21],

and Peña and Reuhkamaa [23] derived stability-dependent wake decay coefficients for infinite wind farm models. These studies collectively establish that atmospheric stability is a first-order influence on wind farm performance.

Terrain effects on wind flow have been studied using a variety of numerical approaches [24]. Chamorro and Porté-Agel [24, 25] provided foundational wind tunnel measurements of wake recovery under different surface roughness and thermal stability conditions. Yan et al. [26] developed a hierarchical meso-microscale coupling method for wind resource assessment over complex terrain. Notably, Wise et al. [27] used mesoscale–microscale coupled simulations to investigate wind turbine wakes over a mountain ridge under both stable and convective conditions, representing one of the few studies to address terrain–stability interactions directly. However, the computational cost of CFD-based approaches limits the number of terrain–stability combinations that can be explored in a single study.

Analytical wake models offer a complementary perspective: they lack the flow resolution of CFD but can rapidly evaluate performance across a wide parameter space, making them useful for identifying first-order sensitivities and guiding more targeted CFD investigations. Several studies have used analytical models for layout optimization [28–30], multi-fidelity Bayesian optimization [30], and data-driven approaches [31–33]. Open-source frameworks such as FLORIS [34], FLOWERS [35], and TurbOPark [36] implement various wake models from analytical formulations to full LES, enabling evaluation of wind farm layouts across a range of fidelity levels. However, neither framework incorporates explicit terrain and stability-dependent wake expansion corrections in a unified parametric study format. Yet a systematic parametric study using an analytical Gaussian wake model to examine the combined effects of terrain complexity and atmospheric stability on wind farm power across multiple terrain types and stability classes has not been reported. While high-fidelity studies have examined terrain–stability interaction for individual sites [27] or individual stability classes [37, 38], the analytical framework offers the ability to span a broader parameter space and identify which combinations warrant further investigation with resolved simulations.

The present study addresses this gap by conducting a parametric assessment using the Bastankhah and Porté-Agel [6] Gaussian wake model with the Niayifar and Porté-Agel [11] turbulence intensity-dependent expansion rate, augmented by empirical stability and terrain correction factors. Hourly ORsted2 mesoscale dataset (2003–2017) provides the atmospheric inflow profiles. The specific objectives are: (1) to systematically quantify how three terrain

types (free, fully nonconvective) and three stability conditions (stable, neutral, convective) interact to affect wake dynamics and farm power output in a 3×3 parametric matrix, (ii) to separate the contributions of hub-height wind-speed differences and wake recovery rate differences to the overall stability effect by running a matched-velocity sensitivity analysis, (iii) to assess the seasonal variability of farm power output using four representative atmospheric profiles, and (iv) to quantify the sensitivity of power predictions to humidity-corrected air density. The limitations of the analytical approach relative to resolved CFD and LES are explicitly characterized throughout.

The remainder of this paper is organized as follows. Section 2 presents the mathematical formulations, including the Gaussian wake model, wake superposition method, and atmospheric stability parameterization. Section 3 describes the wind farm configuration, terrain representations, and simulation matrix. Section 4 presents validation of the wake model against published data and a RANS simulation. Section 5 discusses the results of the parametric study, matched-velocity analysis, seasonal variation, and humidity sensitivity. Conclusions are drawn in Section 6.

2. Mathematical formulation

2.1. Gaussian wake model

The velocity deficit behind each wind turbine is computed using the Gaussian wake model of Bastankhah and Porté-Agel [8]. This model assumes a self-similar Gaussian distribution of the velocity deficit in the wake cross-section. The normalized velocity deficit at downstream distance x and radial distance r from the wake centreline is

$$\frac{\Delta U}{U_\infty} = \left(1 - \sqrt{1 - \frac{C_T}{8(\sigma/D)^2}}\right) \exp\left(-\frac{r^2}{2\sigma^2}\right) \tag{1}$$

where U_∞ is the freestream velocity, C_T is the thrust coefficient, D is the rotor diameter, and σ is the standard deviation of the Gaussian wake profile. The wake width σ grows linearly with downstream distance according to

$$\sigma(x) = k^* (x - x_0) + \frac{D}{\sqrt{8}} \tag{2}$$

where k^* is the wake expansion rate and x_0 is the length of the near-wake region. Following Niayifar and Porté-Agel [13], the wake expansion rate is related to the local ambient turbulence intensity I by

$$k^* = 0.7\,l \tag{9}$$

The wave-scale length, following the parameterization adopted in the FLOWER framework [30] based on the asymptotic-consistency derivation of Bartoshtsluk and Fortin-Ingol [8], is given by:

$$\lambda_w = \frac{k\,(a_1 l)}{\left[1 + \left(\frac{a_1 l}{2k}\right)^{2}\right]^{1/2}} \tag{10}$$

No wake deficit is applied upstream of the rotor ($x < 0$). For downstream positions in the near-wake region ($0 < x < x_{nw}$), the wake width is clamped to $\sigma = \frac{1}{2}\,D\,c_t$/8, so that the deficit formula (eq. (1)) remains a constant-width Gaussian profile whose magnitude increases toward the rotor. This implementation is consistent with the approach adopted in the FLOWER framework [30].

2.3 Stability and terrain corrections to wake expansion

Atmospheric stability and terrain complexity affect wake recovery primarily through their influence on turbulent mixing intensity. To capture these effects within the analytical framework, the wake expansion rate is modified by empirical correction factors:

$$k_{\text{eff}} = k\,(1 + \alpha_s\, I_{\text{amb}} + \alpha_t\, s_t) \tag{11}$$

where I_{amb} is the ambient turbulence intensity at hub height computed from the MOST profiles, α_s is the stability correction factor, and α_t is the terrain correction factor.

The stability correction factors are calibrated to reproduce the qualitative trends observed in LES studies of stability-dependent wake recovery [24, 46, 17]: $\alpha_s = 0.6$ for stable conditions (reduced turbulent mixing), $\alpha_s = 1.0$ for neutral conditions (reference), and $\alpha_s = 1.6$ for convective conditions (enhanced mixing). The resulting ratio $\alpha_s^{\text{conv}}/\alpha_s^{\text{stab}} = 2.67$ is broadly consistent with the convective-to-stable wake decay coefficient ratios of 2–3 derived by Peña and Barthomeuf [35]. The set k_{eff} varies 0.042–0.049 ($\times$ 1.36, convective to stable) is lower than 2.67 because the MOST-derived I_{amb} partially offsets the correction factor (see section 3.3), but falls within the range of 1.5–3 reported across stability-dependent wake studies [24, 35]. It should be noted that the α_s values of 0.6 and 1.6 are calibrated specifically to

the MOST observed hub-height $\overline{U}$ and hence, which exhibits a counterintuitive stability ordering (stable $\overline{U}$ < neutral $\overline{U}$ < convective $\overline{U}$; see section 3.2). Consequently, κ_t performs a dual role: compensating for the $\overline{U}$ ordering artefact and representing the physical stability effect on wake expansion. It paired with a hub-height $\overline{U}$ model that correctly predicts lower $\overline{U}$ under stable conditions, then κ_t values would require re-calibration.

The terrain correction factors account for additional turbulent mixing generated by terrain features: $\kappa_h = 1.0$ for flat terrain, $\kappa_h = 1.25$ for hilly terrain, and $\kappa_h = 1.5$ for mountainous terrain. These values are guided by wind tunnel measurements showing 30–40% $\overline{U}$ enhancement over ridges [34], 15–40% enhancement from surface roughness transitions [35], and 40–80% enhancement over mountain ridges in mesoscale–microscale coupled simulations [37]. The present values fall within these ranges but represent class-average constants; site-specific calibration against high-fidelity CFD or field measurements would be needed for a particular location.

The multiplicative structure of eq. (1) inherently produces non-additive terrain–stability interactions, which is a structural property of the model consistent with the geometric non-linear interactions observed in LES [37]. Verification of the specific interaction magnitude would require combined CFD simulations.

2.3. Wake superposition

In a wind farm with multiple turbines, the combined velocity deficit at any point is computed using the root-sum-of-squares (RSS) superposition method [38–40]:

$$\frac{\Delta U_{i,\mathrm{tot}}}{U_{\infty}} = \sqrt{\sum_{j=1}^{N_{\mathrm{up}}} \left(\frac{\Delta U_{j,i}}{U_{\infty}} \right)^2} \tag{6}$$

where N_{up} is the number of upstream turbines contributing wakes at the point of interest. The effective velocity seen by each downstream turbine is then $U_{\mathrm{eff},i} = U_{\infty}(1 - \Delta U_{\mathrm{tot},i}/U_{\infty})$. In the present implementation, the wake deficit is evaluated at the hub centre of each downstream turbine (point evaluation at $r = |y_i - y_j|$, $z = z_j$) rather than averaged over the rotor swept area as in the FUGA/RIAM framework [18]. For directly aligned turbines ($r = 0$), the point evaluation overstates the maximum Gaussian deficit, which systematically overpredicts the rotor-averaged velocity deficit by approximately 10–15% at $x = 7D$ downstream, this contributes to the slight overprediction of wake

losses relative to the IEA39 comparison (section 4.6). The power output of each turbine is

$$P = \frac{1}{2}\rho C_P A_d U_{\infty}^3 \tag{7}$$

where ρ is the air density, C_P is the power coefficient, and $A_d = \pi D^2/4$ is the rotor swept area. The thrust and power coefficients are specified as functions of the effective velocity based on the NREL 5-MW reference turbine operating characterization [37], with $C_T \approx 0.77$ and $C_P \approx 0.481$ in the below-rated region ($U_{\infty} < 11.4\,m/s$). Since all hub-height wind speeds in the present study fall within the below-rated operating range (7.7–$10.6\,m/s$; table 3), the use of constant C_T and C_P is a reasonable simplification; the NREL 5-MW reference turbine exhibits nearly constant operating coefficients in this region [37]. However, wake-affected turbines in downstream rows may operate at substantially reduced velocities (as low as $\sim 6.5\,m/s$ under stable conditions with cumulative wake deficits of $\sim 40\%$), approaching the cut-in speed of $3\,m/s$. In this low-velocity regime, the turbine controller may not maintain the optimal tip-speed ratio, and the constant-coefficient assumption may introduce additional error in the power estimates for heavily wake-affected turbines. A realistic $C_P(U)$ curve for the NREL 5-MW turbine would exhibit reduced thrust and power coefficients below approximately $7\,m/s$. Further decreasing flow U_{∞} power under stable conditions, consequently, the reported 20% wake loss for the stable fast-terrain case should be interpreted as a lower bound on the actual wake-induced power reduction.

2.4 Atmospheric boundary layer profile

The atmospheric inflow conditions are prescribed using Monin–Obukhov similarity theory (MOST) [38]. The mean streamwise velocity profile is

$$U(z) = \frac{u_*}{\kappa}\left[\ln\left(\frac{z}{z_0}\right) - \psi_m\left(\frac{z}{L}\right)\right] \tag{8}$$

where u_* is the friction velocity, $\kappa = 0.4$ is the von Kármán constant, z_0 is the aerodynamic roughness length, L is the Obukhov length, and ψ_m is the integrated stability correction function for momentum. For stable conditions ($L > 0$), the Businger–Dyer functions [39] $\psi_m = -\gamma z/L$ are employed. For unstable conditions ($L < 0$), the Paulson [40] formulation is used.

$$\alpha_{\rm ts} = \beta\ln\!\left(\frac{1+\beta}{\beta}\right) - \ln\!\left(\frac{1+\beta}{\beta}\right) - 2\,\mathrm{arctan}(\beta) + \frac{\pi}{2} \qquad \beta = (1-\mathrm{Ri}_{\rm f})/\mathrm{Ri}_{\rm f}^{1/2}. \tag{A}$$

The turbulent kinetic energy at hub height, needed to compute the ambient turbulence intensity $I_{\rm amb} = \sqrt{(2k/3)}/U_{\rm hub}$, is derived from the local equilibrium assumption:

$$k(z) = \frac{u_*^2}{\sqrt{C_\mu}}\,\alpha_{\rm ts}(z/L), \tag{A8}$$

where $C_\mu = 0.09$ and $\alpha_{\rm ts} = 1 + 5\,z/L$ for stable and $\alpha_{\rm ts} = (1-16\,z/L)^{-1/4}$ for unstable conditions. Equation (A8) represents the local-equilibrium assumption and is strictly valid only within the surface layer (typically $z < 0.1\,h$, where h is the ABL height). Since the hub height ($z_{\rm hub} = 90\,\mathrm{m}$) may exceed the surface-layer depth under stable conditions ($0.1\,h = 30\,\mathrm{m}$ for $h = 300\,\mathrm{m}$), an exponential decay factor is applied above the surface layer:

$$k(z) = \frac{u_*^2}{\sqrt{C_\mu}}\,\alpha_{\rm ts}(z/L)\,\exp\!\left[-\,d\,\frac{\max(z) - 0.1\,h}{h}\right] \tag{A9}$$

The decay coefficient of 3 provides a smooth reduction of TKE above the surface layer, recognizing that the local-equilibrium assumption progressively deteriorates with height [64]. This correction reduces hub-height TKE by approximately 15% under stable conditions while having no effect under convective conditions (where $0.1\,h < 150\,\mathrm{m} < z_{\rm hub}$).

2.2 Vertical wake profile extension

The Bastankhah and Porté-Agel [6] Gaussian wake model assumes a rotationally symmetric deficit profile in the wake cross-section, with a single width parameter σ for both the lateral and vertical directions. To generate vertical wake profiles for visualization (figs. 14 to 15), we extend this by applying a separate vertical Gaussian envelope to the hub-height deficit:

$$\frac{\Delta U(z,\,y,\,z)}{U_\infty} = \frac{\Delta U(z,\,y,\,z_{\rm hub})}{U_\infty}\,\exp\!\left[-\,\frac{(z-z_{\rm hub})^2}{2\,\sigma_z^2}\right] \tag{A10}$$

where the vertical wake width is parameterized as

$$w_{\mathrm{eff}}(x) = \begin{cases} w_0 & x \le x_0 \\ w_0 + \alpha_w \left(\dfrac{x - x_0}{x_{\mathrm{ref}}}\right)^{p_w} & x > x_0 \end{cases} \tag{116}$$

This parameterization allows the vertical scale width to grow with downstream distance at a rate that depends on the effective mixing intensity, analogous to the lateral growth rate. The coefficients are chosen to produce a scale aspect ratio near unity at mesoscale downstream distances ($x \sim 2^{p_w} - 1$ x_0), consistent with the constrained symmetric assumption of the original Gaussian model. It is acknowledged that this extension breaks the strict rotational symmetry of the Bastankhah and Porté-Agel [6] formulation and introduces additional empiricism; the vertical profiles should therefore be interpreted as qualitative illustrations of the stability-dependent vertical scale structure rather than quantitative predictions.

2.6 Humidity correction for air density

Air density depends on temperature, pressure, and humidity through the equation of state for moist air [33]. The density of humid air is approximated by:

$$\rho = \frac{p - e}{R_d T} + \frac{e}{R_v T} \tag{118}$$

where p is the atmospheric pressure, T is the absolute temperature, e is the water vapour partial pressure, $R_d = 287.058\,\mathrm{J/(kg\cdot K)}$ is the specific gas constant for dry air, and $R_v = 461.495\,\mathrm{J/(kg\cdot K)}$ is the specific gas constant for water vapour. The vapour pressure is computed from the relative humidity RH and the saturation vapour pressure $e_s(T)$ using the Buck equation:

$$e = \mathrm{RH} \cdot e_s(T), \qquad e_s = 611.21 \cdot \exp\!\left[\frac{\left(18.678 - \frac{T_c}{234.5}\right) T_c}{257.14 + T_c}\right], \tag{119}$$

where $T_c = T - 273.15$ is the temperature in degrees Celsius. Since water vapour is less dense than dry air at the same temperature and pressure, increasing humidity reduces air density and consequently reduces turbine power output, which is proportional to ρ (eq. 77).

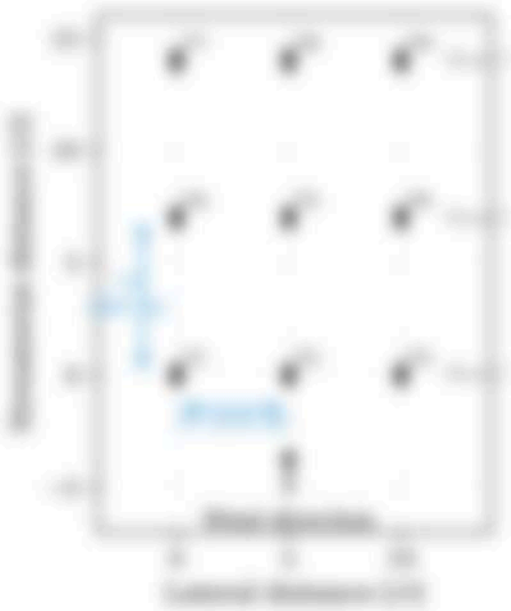

Figure 1. Schematic of the 3 × 3 wind farm layout, showing nine NREL 1.4MW turbines with streamwise spacing of 7D and lateral spacing of 5D.

2. Wind farm configuration and simulation matrix

2.1. Wind farm layout and turbine specifications

The wind farm consists of nine NREL 1.4MW reference turbines [27] arranged in a 3×3 grid with streamwise spacing of 7D and lateral spacing of 5D, where $D = 130$ m is the rotor diameter and the hub height is $z_h = 90$ m. This layout, shown schematically in fig. 1, represents a typical medium-density wind farm configuration and produces significant wake interactions between successive turbine rows. The turbine and layout parameters are listed in table 1.

2.2. Terrain representations

Three terrain types are considered to span the range of topographic complexity encountered in wind energy applications. The terrain representations are idealized functional forms designed to capture the key features of each terrain class without attempting to reproduce specific real-world topographies.

The *flat* terrain consists of a smooth horizontal surface with a uniform aerodynamic roughness length $z_0 = 0.001$ m, representative of open agricul-

Table 1. Turbine specifications and wind farm layout parameters.

Parameter	Value	Unit
NREL 1.4 MW reference turbine		
Rotor diameter D	126	m
Hub height z_h	90	m
Rated power	1.4	MW
Cut-in, rated, cut-out wind speed	3, 12.6, 25	m/s
Thrust coefficient C_T (below rated)	0.77	–
Power coefficient C_P (below rated)	0.483	–
Wind farm layout		
Configuration	5×5 grid	–
Streamwise spacing	$7D$ (882 m)	m
Lateral spacing	$5D$ (630 m)	m
Total turbines	25	–

rated load. This configuration serves as the baseline for isolating the effects of streamwise mobility on wake dynamics.

The hilly terrain is represented by an idealized sinusoidal surface with amplitude $A = 75\,\mathrm{m}$ and wavelength $\lambda = 750\,\mathrm{m}$, producing gentle rolling hills characteristic of many onshore wind farm sites. The terrain elevation is given by $z_s(x, y) = A\sin(2\pi x/\lambda)\cos(2\pi y/\lambda)$, generating alternating ridges and valleys oriented perpendicular to the prevailing wind direction. In the analytical model, this terrain is represented through the terrain correction factor $\alpha_t = 1.25$ (eq. (7)) rather than through explicit flow resolution; the factor captures the empirical observation that hilly terrain increases ambient turbulence intensity and thereby accelerates wake recovery.

The nonstationary terrain is generated using a superposition of two sinusoidal modes with amplitudes $A_1 = 200\,\mathrm{m}$, $A_2 = 150\,\mathrm{m}$ and wavelengths $\lambda_1 = 1000\,\mathrm{m}$, $\lambda_2 = 600\,\mathrm{m}$. The corresponding terrain correction factor is $\alpha_t = 1.5$. The analytical model does not resolve terrain-induced flow separation or channelling; it captures only the net effect of terrain on turbulent mixing intensity. A uniform roughness length $z_0 = 0.03\,\mathrm{m}$ is used for all three terrain types, isolating the terrain mixing effect through α_t in reality, nonstationary terrain would exhibit higher roughness ($z_0 \sim 0.3$–$1.0\,\mathrm{m}$), which would further modify the inflow conditions. The three terrain profiles are

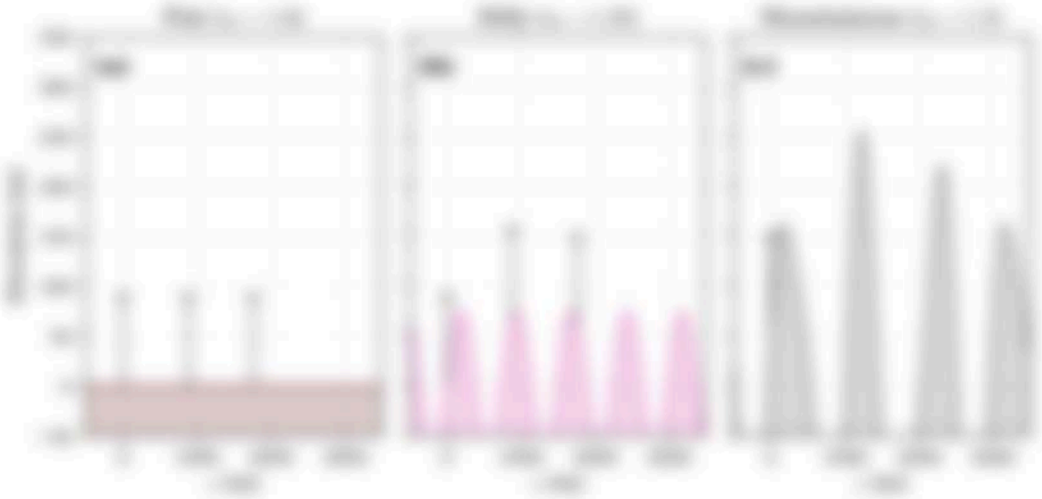

Figure 4: Cross-sectional terrain profiles for the three terrain types considered: (a) flat, (b) hills, and (c) mountainous. Vertical lines indicate orthogonal turbine locations. The terrain correction factors c_t used in eq. (1) are stated for each type.

illustrated in fig. 3

2.3 Atmospheric conditions

The atmospheric boundary layer parameters for each stability class are summarized in table 2. The hub-height wind speed and turbulence intensity for each condition are derived from the MOST profiles (eqs. (8) and (10)) and are listed in the table for reference.

The resulting velocity and turbulence intensity profiles are shown in fig. 5

Table 3. Aerodynamic-condition parameters for the three mobility classes.[a]

Parameter	Stable	Neutral	Convective
Friction velocity u_* [m s^{-1}]	0.30	0.45	0.55
Obukhov length L [m]	400	∞	-400
Surface roughness z_0 [m]	0.03	0.03	0.03
ABL height h [m]	500	1000	1500
Surface temperature θ_s [K]	290	300	310
Bulk-height wind speed U_z [m s^{-1}]	7.7	9.0	10.0
Bulk height M [$\mathrm{kg\,m^{-1}\,s^{-2}}$]	6.7	7.4	8.3
Stability correction ψ_z	5.0	1.0	-1.0

[a] Bulk-height values derived from MOST profiles (eqs. 10 and 11).

[b] The 10 achieving results — neutral — convective) to conservative and arises from the z_0 amplification of TKE to u_* (11) at heights that may current the surface-layer depth under stable conditions are discussion in section 4.3. The physically correct stability-dependent wake recovery is restored by the ψ_z correction factors.

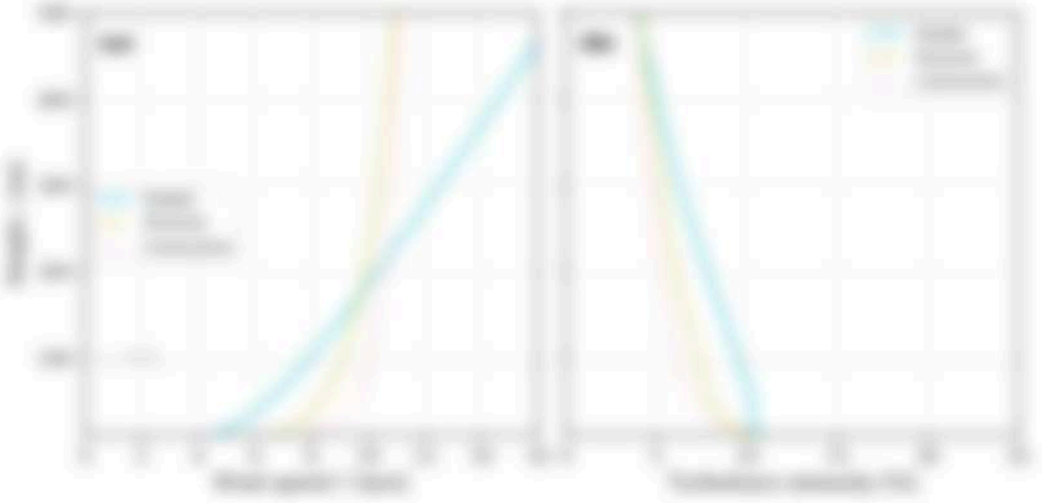

Figure 4. Aerodynamic inspection layer profiles for the three mobility conditions. (a) mean streamwise velocity and (b) turbulence intensity as functions of height. The dashed layer control line indicates the hub height $z_h = 90$ m.

The hub-height TI values in table 3 display a counterintuitive ordering (stable > neutral > convective), arising because $u_{*0}/|z-z_0|$ amplifies in stable stratification at heights exceeding the surface-layer depth. This is a known limitation of applying the local-equilibrium TKE assumption at hub height [63]. An exponential decay factor ($\propto e^{-z/L}$) partially corrects for this. The physically correct stability-dependent wake recovery is restored by the c_{t_0} factors, which produce effective wake expansion rates increasing from stable ($k_{w_0} = 0.026$) to neutral (0.047) to convective (0.054), consistent with LES observations [64, 65].

An important caveat of this setup is that the three stability conditions correspond to different hub-height wind speeds (7.7, 9.0, and 10.0 m s^{-1}), because IEC 61400 prescribes the velocity profile as a function of z_0, z_h, and I. Since power scales with the cube of wind speed, the resulting power differences across stability classes reflect the combined effects of freestream velocity and wake recovery rate, not stability effects in isolation. To disentangle these effects, a matched-velocity sensitivity analysis is presented in section 5.4, following the approach advocated by Du et al. [66] for properly controlled stability comparisons.

3.3. Simulation matrix

The full simulation matrix comprises 30 cases, as summarized in table 4. The nine primary cases (C1–C9) form the 3×3 parametric matrix of terrain types and stability conditions. Three matched-velocity cases (M1–M3) isolate the stability effect on wake recovery by holding the hub-height wind speed constant at 9.0 m s^{-1} across all three stability conditions on flat terrain. Four humidity sensitivity cases (H1–H4) assess the effect of humidity-corrected air density at relative humidity levels of 20%, 40%, 60%, and 80%.

4. Validation

4.1. BANSE mesh convergence study

A mesh convergence study is conducted for the single actuator disk BANSE simulation under neutral conditions to assess the sensitivity of the wake predictions to grid resolution. Three structured hexahedral meshes are considered: a coarse mesh ($80 \times 40 \times 30 = 96{,}000$ cells), a medium mesh ($120 \times 60 \times 45 = 324{,}000$ cells), and a fine mesh ($180 \times 90 \times 60 = 972{,}000$ cells). The mesh refinement ratio between consecutive levels is approximately 1.5 in each direction. All three simulations use identical boundary conditions,

Table 3. Baseline matrix: primary, matched-velocity, and sensitivity cases.

Case	Formula	Stability	Purpose
C1	Flat	Stable	Parametric matrix
C2	Flat	Neutral	Baseline reference
C3	Flat	Convective	Parametric matrix
C4	Hills	Stable	Parametric matrix
C5	Hills	Neutral	Parametric matrix
C6	Hills	Convective	Parametric matrix
C7	Mountainous	Stable	Parametric matrix
C8	Mountainous	Neutral	Parametric matrix
C9	Mountainous	Convective	Parametric matrix
M1	Flat	Stable	Matched velocity $(U_h = 9.0$ m s$^{-1})$
M2	Flat	Neutral	Matched velocity $(U_h = 9.0$ m s$^{-1})$
M3	Flat	Convective	Matched velocity $(U_h = 9.0$ m s$^{-1})$
S1–S4	Flat	Neutral	Resolution: 800 / 40 / 20 / 10 m

solver settings (`simpleFoam`, standard k–ε, and actuator-disk parameters, and all converge within 150 iterations with residuals below 10^{-5}.

Figure 4 compares the centerline wake velocity deficit and the lateral wake profile at $x/D = 7$ across the three mesh levels. The coarse and medium meshes show discernible differences in the centerline deficit, particularly at $x/D = 3$–7 where the velocity gradient across the wake is steepest. The medium and fine meshes converge to within 3% of each other at all downstream stations, indicating that the medium mesh is approaching grid independence for the mean velocity field. The lateral profile comparison at $x/D = 7$ confirms this trend: the coarse mesh produces a broader, shallower wake (consistent with its lower spatial resolution smoothing the velocity gradients), while the medium and fine meshes yield nearly identical profiles.

A Richardson extrapolation is performed using the centerline velocity at $x/D = 7$ to estimate the grid convergence index (GCI). With the coarse-to-medium-to-fine mesh triplet and a refinement ratio $r = 1.5$, the observed order of convergence is approximately 1.8, consistent with second-order spatial discretization. The GCI for the fine mesh is 1.2%, indicating that the fine-mesh solution is within 1.2% of the asymptotic grid-independent value. The single-turbine RANS validation under neutral conditions (section 4.1) is

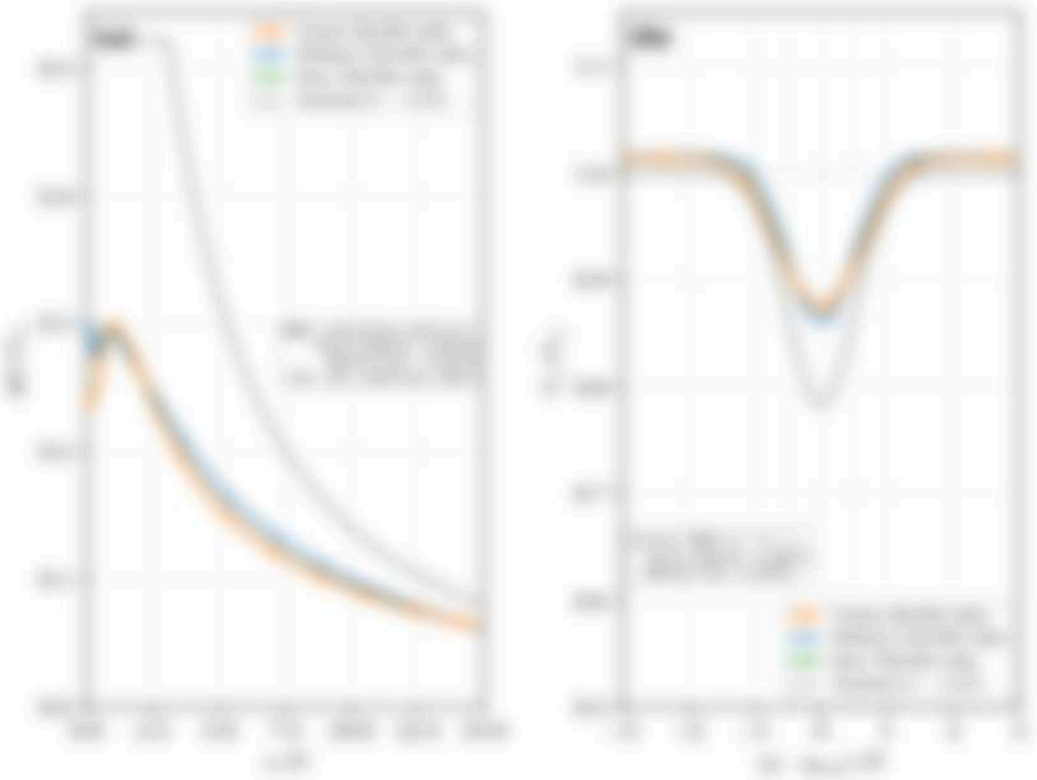

Figure 4. Mesh convergence study for the single aerogenerator Mid-RANS simulations under uniform conditions. (a) centerline velocity deficit $\Delta U/U_\infty$ for three mesh levels (Min, Mid, and Max cells) and the analytical Gaussian model; (b) lateral velocity profile at $x/D = 7$ for the three mesh levels and the analytical model. Vertical dashed lines in (b) indicate rotor edges.

performed on the fine mesh ($160 \times 80 \times 40$, GCI $\approx 1.3\%$), ensuring that the analytical RANS comparisons is not confounded by mesh uncertainty. The farm-level RANS comparisons (sections 4.3) uses a coarser mesh, as noted in the respective sections. The mesh convergence data are reported to allow the reader to assess the numerical uncertainty of the RANS reference solutions directly.

4.1 Single-turbine wake profiles

The Gaussian wake model is validated for single-turbine wake predictions by comparing the predicted centerline velocity deficit against published experimental and numerical data. Bastankhah and Porté-Agel [8] validated

the model extensively against wind tunnel measurements of separation vortex wakes at downstream distances of $x/D = 1$–20, demonstrating that the Gaussian deficit profile agrees with the measured lateral velocity distribution to within 1–10% for $x/D \geq 4$. The model underpredicts the deficit in the near-wake region ($x/D < 3$), where the wake has not yet transitioned to a self-similar Gaussian profile.

Figure 5.1(a) compares the centerline velocity deficit predicted by the present implementation ($k^* = 0.040$) against the model-level predictions of Bastankhah and Porté-Agel [B, $k^* = 0.038$] and Ishihara and Qian [IQ, $k^* = 0.052$] for a single turbine under neutral conditions ($C_T = 0.77$, $I = 0.06$). The shaded band represents a synthetic $\pm 10\%$ envelope corresponding to the typical across-source range reported by Bastankhah and Porté-Agel [B] for $x/D = 4$–20. The three curves span the range of k^* values in the literature, demonstrating that the wake expansion rate has a first-order effect on the deficit. Figure 5.1(b) shows the sensitivity over the modelling-relevant range $k^* = 0.025$–0.060, consistent with the modelling-dependent wake-decay rates reported in LES studies [14, 15].

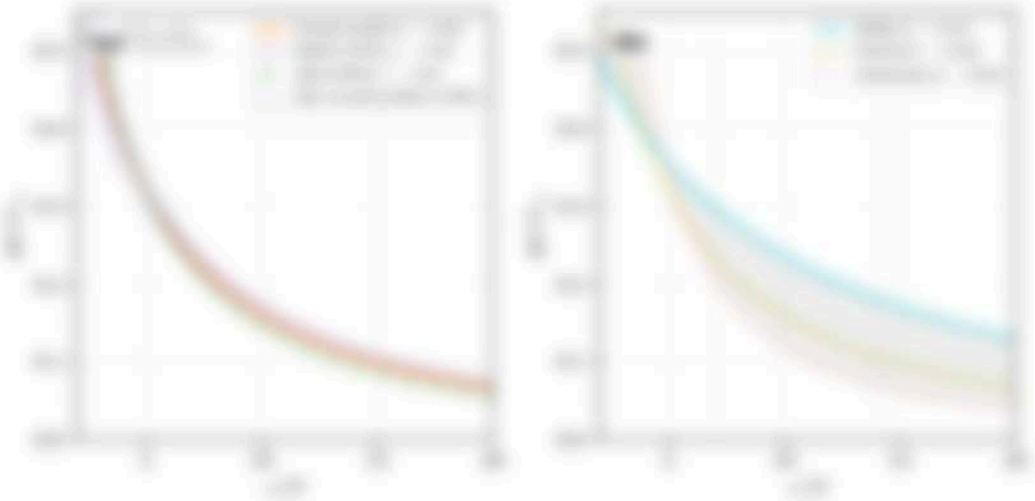

Figure 5. Validation of the Gaussian wake model. (a) centerline velocity deficit for a single turbine under uniform conditions, comparing the present model (solid line, $A' = 0.5666$) with the analytical predictions of Bastankhah and Porté-Agel [6] (dashed, $A' = 0.6000$) and Ishihara and Qian [18] (dash-dotted, $A' = 0.5985$); the shaded band represents a synthetic $\pm 10\%$ envelope around the present model's prediction, corresponding to the typical accuracy range reported by Bastankhah and Porté-Agel [6] in their wind tunnel validation for $x/D > 3$. (b) quantitative analytical-only cut from representative farm results. Evolution of the centerline deficit κ for the wake expansion rate $k^* = 0.04$ corresponding to results of $k^* = 0.0413$, assisted ($k^* = 0.0496$), and convective ($k^* = 0.0289$) conditions, with the shaded regions denoting the full stability-dependent range.

4.3 Wake superposition and farm power

For multi-turbine configurations, the RSS wake superposition method has been validated against 90 3210 hours from the Horns Rev 1 offshore wind farm by Barthelmie et al. [20, 18]. The Gaussian model with RSS superposition typically predicts row-averaged power deficits within 38 4.5% of the measured values for aligned flow conditions, with the accuracy depending on the choice of wake expansion rate [14]. The model tends to underpredict wake losses for closely spaced turbines ($s/D < 5D$) and overpredict them for widely spaced layouts ($s/D > 10D$), consistent with the known limitations of the Gaussian self-similarity assumption in the near wake and far wake regions [6, 18].

4.4 Stability-dependent trends

The stability-dependent behaviour of the model is assessed by comparing the relative farm power output across the three stability conditions against

qualitative trends reported in the literature. Under stable stratification, the present model predicts a farm power that is 40% lower than the neutral baseline, while convective conditions yield a 40% increase. As noted in section 3.2, these differences arise from the combined effects of different hub-height wind speeds and stability-dependent wake recovery rates, rather than from stability effects in isolation. The direction and approximate magnitude of the stability-driven power variation are consistent with the 20–25% range of power deficits under stable conditions reported in the field measurement and LES literature [14, 15, 16]. A more rigorous isolation of stability effects, matching hub-height wind speed across all conditions as done by Du et al. [16], is presented in section 3.4.

4.3. Comparison with RANS simulation

To provide a direct numerical reference for the analytical wake predictions, a steady-state RANS simulation is performed using OpenFOAM [18] for a single NREL 5 MW actuator disk under the neutral baseline conditions. The solver `simpleFoam` is employed with the standard $k-\varepsilon$ turbulence model and wall functions. The computational domain is $2520 \times 1260 \times 630\,\mathrm{m}$ ($20D \times 10D \times 5H$), discretized with the bias structured hexahedral mesh of $400 \times 40 \times 60 = 700{,}000$ cells (approximately 8 cells per rotor diameter in the lateral and vertical directions), which is the finest mesh from the convergence study (section 4.1), with a GCI of 1.3% relative to the grid-independent solution. The turbine is represented as an actuator disk using the `actuatorDiskSource` model with $C_T = 0.77$ and rotor area $A_r = 12{,}469\,\mathrm{m}^2$. The actuator disk applies a uniform momentum sink across the rotor plane, producing an axisymmetric wake without radial load variation, wake rotation, or tip vortices. This is a deliberate choice: the Gaussian wake model also assumes an axisymmetric deficit profile, so the RANS comparison tests the wake recovery prediction under a consistent set of simplifying assumptions rather than introducing additional physics (e.g., resolved blade loading) that the analytical model cannot capture. The inlet boundary conditions uses the `atmBoundaryLayerInletVelocity` profile with $U_{\mathrm{ref}} = 9.0\,\mathrm{m/s}$ at $z_{\mathrm{ref}} = 90\,\mathrm{m}$ and $z_0 = 0.05\,\mathrm{m}$. The simulation converges within 176 iterations (residuals below 10^{-4}).

Figure 4(a) shows the hub-height horizontal plane of the normalized streamwise velocity U_x/U_∞ from the RANS simulation, revealing a well-defined wake extending more than 10D downstream. The wake structure exhibits the expected gradual recovery with downstream distance, and the

contour lines at $U_{wake}/U_{\infty} = 0.90$, 0.96, and 0.99 delineate the wake boundaries. The measured inflow velocity at hub height (averaged over cells upstream of the turbine) is $U_{\infty} = 8.0\,m/s$, slightly below the prescribed inlet reference velocity of $8.01\,m/s$ due to the numerical development of the atmospheric boundary layer profile within the computational domain.

Figure 6(b) compares the lateral wake velocity profiles extracted from the RANS simulation at $x/D = 1$, 7, and 10 against the Gaussian wake model predictions. At all three stations, the RANS simulation predicts a broader and shallower wake than the Gaussian model, consistent with the known tendency of the standard $k-\varepsilon$ model to overpredict turbulent mixing and hence accelerate wake recovery [5]. Quantitative error metrics for the lateral profiles within $y/j = \pm D$ are summarized in table 4. The root-mean-square error (RMSE) between the analytical and RANS profiles decreases from 0.049 at $x/D = 1$ to 0.013 at $x/D = 10$, reflecting improved agreement in the far wake where both models converge toward the freestream. The centerline velocity deficit predicted by the Gaussian model exceeds the RANS value at all stations: the analytical model predicts deficits of 0.497, 0.772, and 0.895 at $x/D = 1$, 7, and 10, while the RANS simulation yields 0.427, 0.745, and 0.891, respectively. The fine mesh resolution (approximately 8 cells per rotor diameter) reduces the numerical diffusion relative to the coarse mesh, and the RANS-predicted centerline deficits are correspondingly deeper than those obtained on the coarse mesh (section 5.1), narrowing the analytical–RANS discrepancy. This remaining systematic overprediction of the deficit by the analytical model (equivalently, underprediction by the RANS) is attributable to the excessive turbulent diffusion inherent to the standard $k-\varepsilon$ model [5], which is known to overestimate wake recovery rates compared to both measurements and LES. Ishihara-Qian-Rivera et al. [5] demonstrated that the standard $k-\varepsilon$ model can overpredict wake recovery by 30–50% relative to their corrected formulation; the present discrepancy is consistent with this finding.

It is important to interpret these error metrics with appropriate caution. The comparison demonstrates consistency between two independent modelling approaches rather than validation of either against ground truth. The fine mesh resolution (approximately 8 cells across the rotor diameter) provides a GCI of 1.2% relative to the grid-independent solution (section 5.1), ensuring that the RANS results are well converged and that the remaining discrepancy with the analytical model is attributable to the turbulence closure rather than to mesh resolution. The standard $k-\varepsilon$ model is itself

Table 4. Quantitative comparison of analytical Gaussian wake model and RANS results for lateral profiles within $y/r = \pm 3$ for both neutral and stable inflow conditions[a]

Condition	z/H	RMSE	SSE	Centerline deficit		$\Gamma_{2,0}$	Deficit error		$\Gamma_{2,\mathrm{RMS}}$
				Analytical	RANS		(Γ_1)		[m/s]
Neutral	1	0.0459	0.0421	0.316	0.306		30		—
	7	0.0364	0.0265	0.317	0.316		85		—
	20	0.0413	0.0340	0.320	0.313		25		—
Stable[b]	1	0.054	0.045	0.345	0.376		86		7.78
	7	0.036	0.025	0.356	0.345		85		7.78
	20	0.049	0.014	0.362	0.315		41		7.86

[a] Profiles are normalized by local freestream velocity at each station.

[b] Both neutral and stable comparisons use the fine mesh ($160 \times 80 \times 48$, 768k cells). The stable deficit errors are comparable to the neutral errors; the fine mesh substantially reduces the discrepancy relative to the coarse mesh (centerline errors decrease from 207 m/s to 41 m/s). The $\Gamma_{2,\mathrm{RMS}}$ column lists the local freestream velocity at each station, so the fine mesh, the stable boundary layer develops only modestly ($\approx 1.5\%$ freestream variation from $z/H = 1$ to 16), compared to 10% on the coarse mesh.

an imperfect reference, as its extrapolation of turbulent mixing in wake flows is well documented [7, 8]. Nevertheless, both approaches predict qualitatively similar wake structures—a Gaussian-like lateral deficit profile that narrows and deepens with increasing downstream distance—and the RMSE of 0.013–0.059 on the normalized velocity provides a quantitative measure of the discrepancy between the two modelling frameworks for this single-turbine neutral case.

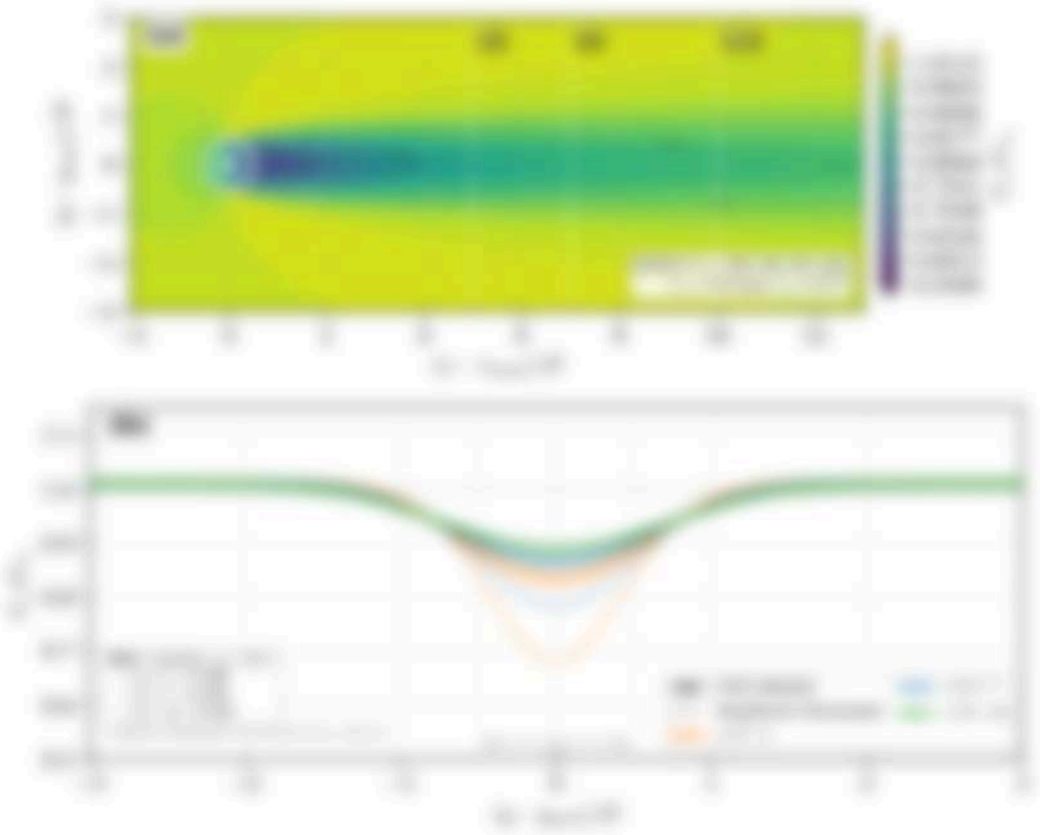

Figure 4. Comparison of RANS simulation and analytical Couette–wake model for a single VAWT. (a) RANS streamwise wake velocity contours for the full-height normalized streamwise velocity field from OpenFOAM (simpleFoam, k–ω SST, $\Delta t = 0.1$ s, 2000 s). Solid white contour lines indicate $U_x/U_\infty = 0.90$, 0.80, and 0.70, dashed vertical lines mark the profile extraction locations at $x/D = 1$, 3, and 10. (b) Lateral wake profiles at $x/D = 1$, 3, 7, and 10, comparing RANS (symbols with solid lines) and Gaussian model (dashed lines). Vertical dotted lines indicate the rotor edges ($z/D \pm 0.5$). The measured inflow velocity is $U_\infty = 10.0$ m/s (generalized inlet). Setup in [1].

4.4. Wind farm ALM/LES validation

To validate the RNS wake superposition method (eq. 16) at the farm level, a second ALM/LES simulation is performed for the full 3×3 wind farm under neutral conditions using OpenFOAM. The computational domain is $6500 \times 2520 \times 1000$m, discretized with a structured mesh of $130 \times 60 \times 46 = 374{,}000$ cells. Nine actuator disks are placed at the positions defined in section 3.1, with streamwise spacing of $5D$ and lateral spacing of $3D$. The same solver configuration (simpleFoam, standard $k-\varepsilon$ atmospheric inlet profile) is used as in the single-turbine case. The simulation converges within 480 iterations with residuals below 10^{-5}.

Figure 7(a) shows the hub-height normalized velocity field for the nine-turbine configuration. The wake interactions between successive rows are clearly visible: downstream turbines operate in the merged wakes of upstream rows, producing progressively deeper velocity deficits. The centerline turbine column exhibits the strongest wake interactions due to direct wake impingement, while the outer columns benefit partially from lateral wake edge effects.

Figure 7(b) compares the row-averaged power per turbine between the ALM/LES simulation and the analytical Gaussian model. The ALM/LES predicts a total farm power of ≈ 6.46 MW, while the analytical model predicts ≈ 7.1 MW, a difference of $\sim 1.2\%$. At the row level, the front row shows the largest discrepancy ($\sim +2.2\%$), because the ALM/LES inflow velocity at the first turbine row is slightly lower than the freestream due to the actuator disk back-pressure effect, which the analytical model does not capture. The middle row shows a $\sim -6.8\%$ difference, and the rear row shows a $\sim +1.8\%$ difference. The sign reversal between the front row ($+2.2\%$) and the middle row (-6.8%) can be understood as follows: the analytical model does not account for the blockage-induced velocity reduction upstream of the rotor, which causes it to overestimate the inflow velocity (and hence power) at Row 1. At Row 2, this blockage effect is offset by the interaction of deeper individual wake deficits predicted by the Gaussian model (section 4.3), which accumulate through the RMS superposition to produce a cumulative deficit exceeding the ALM/LES prediction. effectively, the Gaussian model's tendency to overpredict individual wake deficits dominates the Row 2 comparison, while the absence of blockage modelling dominates the Row 1 comparison. At Row 3, the compounding of both partially cancel, yielding a smaller net discrepancy. Quantitatively, the power at each downstream row depends on $C_{T_{\text{eff}}}$, so even modest differences in the cumulative velocity deficit are amplified through the cubic depen-

down. The transition from overprediction at Row 1 to underprediction at Row 3 therefore reflects a crossover between two competing wake sources: the absence of blockage (which inflates the Gaussian model's prediction at all rows) and the overprediction of individual wake deficits (which accumulates through RSS superposition and progressively deepens the cumulative deficit at downstream rows). This interplay is a structural consequence of comparing a superposition-based analytical model against a fully coupled RANS solution and would not necessarily persist under different turbine spacings or inflow conditions. The overall agreement within $\pm 12\%$ at the row level and $\pm 3\%$ at the farm level provides a quantitative measure of the discrepancy between the two modelling frameworks for a multi-turbine array case. This level of agreement is comparable to the 10–15% accuracy reported for Gaussian wake models applied to the Horns Rev 1 wind farm [40, 12].

The farm mesh (270,000 cells, approximately 4 cells per rotor diameter laterally) is coarser than the fine mesh used for the single-turbine comparison (section 4.1), and no grid convergence index was computed for the farm configuration. Extrapolating from the single-turbine mesh convergence study (section 4.1), which shows approximately 5% uncertainty in the wake deficit on a comparable density mesh relative to grid-independent values, the farm-level $\pm 3\%$ power agreement should be interpreted cautiously, as some of the analytical–RANS difference may be attributable to mesh resolution rather than model differences. A farm-level simulation on the fine mesh would reduce this uncertainty but at substantially increased computational cost. Furthermore, both the single-turbine and farm RANS simulations are run level to neutral conditions on flat terrain. A comparison under stable inflow conditions is presented in section 4.9, but the stability correction factors (α_{ti}) and terrain correction factors (α_{θ}) have not been validated against thermally stratified CFD, extending the RANS comparison to buoyancy-coupled inflows and terrain-conforming meshes remains a priority for future work.

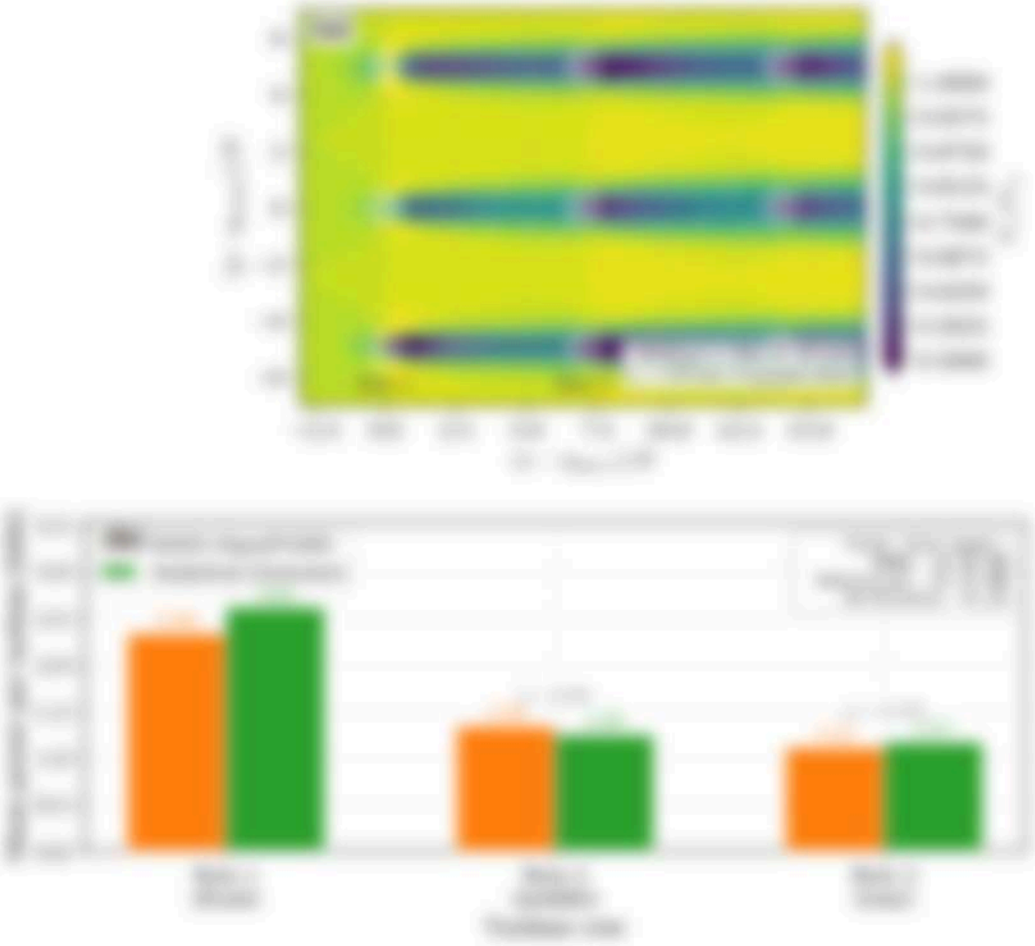
Case 1
Case 2
Case 3
Wall
Wall
Wall

4.1. Three-dimensional wake structure

Figure 8 presents the three-dimensional wake structure from the neutral RANS simulation on the coarse mesh ($30 \times 40 \times 30 = 36{,}000$ cells), which provides sufficient resolution for qualitative visualization of the wake topology. Illustrating the spatial extent and recovery of the actuator disk wake. The hub-height horizontal cross-section reveals the classical elongated wake deficit, while the vertical cross-section through the wake centerline shows the vertical spread of the velocity deficit and its interaction with the atmospheric boundary layer profile. The isosurface visualization at $U_{\infty}/U_{\infty} = 0.80$ delineates the three-dimensional wake boundary, confirming that the wake extends approximately 1027 downstream before recovering to within 20% of the freestream velocity.

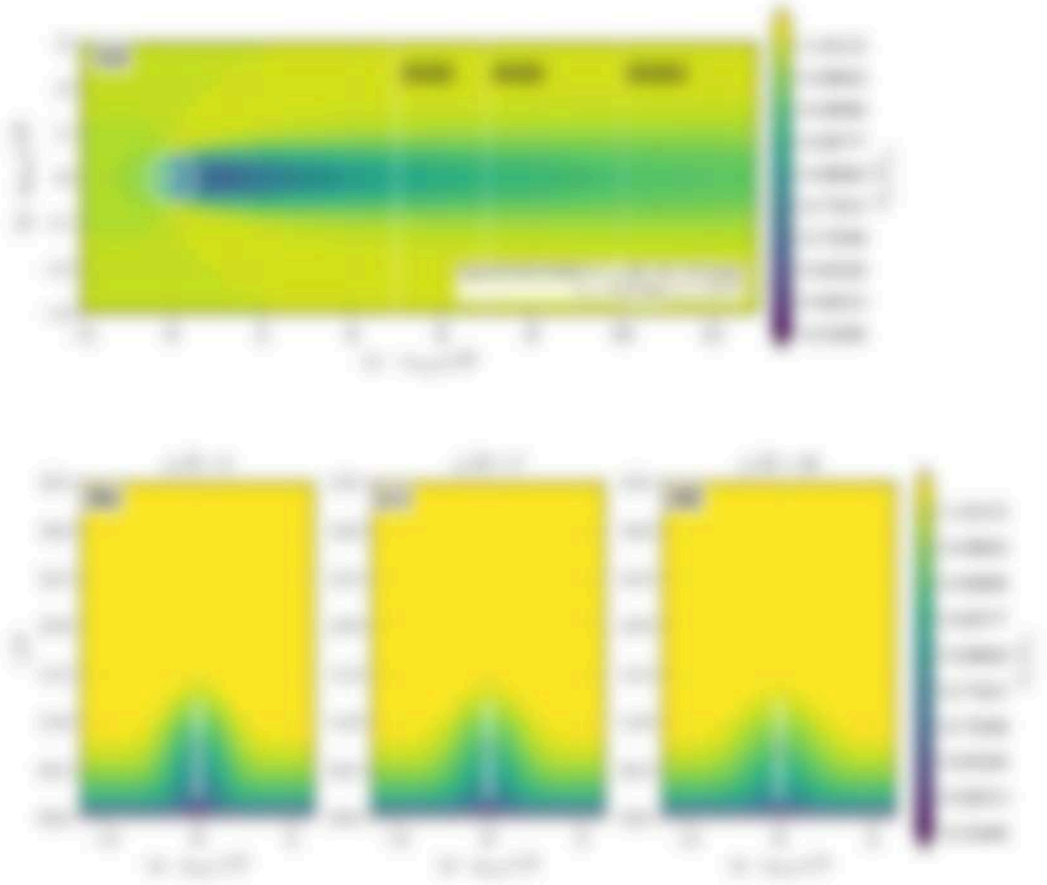

Figure 4. Three-dimensional wake structure from the RANS actuator disk simulation under nominal conditions on the coarse mesh ($\Delta x = \Delta z = 50$ m cells). (a) isosurface of $U_x/U_{x_\infty} = 0.90$ coloured by height, showing the upstream extent of the wake. (b) vertical cross-section at $y = y_{\mathrm{hub}}$ of the normalised streamwise velocity. (c) hub-height horizontal cross-section of the normalised streamwise velocity. The rotating disk location is marked in each panel. This mesh is coarser than the fine mesh used for quantitative wake profile comparisons (Figs. 5 and 6).

4.4. Stable inflow RANS comparison

To assess the model-level wake model's predictions under non-neutral inflow conditions, a RANS simulation is performed using OpenFOAM for the single actuator disk case with a stable atmospheric boundary layer inlet profile. The inlet velocity is prescribed using the MOST profile (eq. 35) with $u_* = 0.30\,\mathrm{m\,s^{-1}}$, $L = 200\,\mathrm{m}$, and $z_0 = 0.05\,\mathrm{m}$, yielding a hub-height wind speed of $U_h = 7.7\,\mathrm{m\,s^{-1}}$. The same solver configuration (`simpleFoam`, standard k–ε and actuator disk parameters) are used as in the neutral case, on the fine mesh ($160 \times 80 \times 40 = 500{,}000$ cells). The SIMPLE algorithm converges in 458 iterations (tol $= 1$, endTime $= 6000$). All six field residuals fall below 10^{-4}: the U_x, y, and z residuals reach $\mathcal{O}(10^{-5})$–$\mathcal{O}(10^{-6})$, while U_z and k settle at $\mathcal{O}(10^{-5})$–$\mathcal{O}(10^{-6})$, the U_z residual, which is the slowest to converge due to the small magnitude of vertical velocity in flat terrain, finishes 8.0×10^{-5}, just below the 10^{-4} threshold. The downstream velocity variation is less than 1.5% across the domain, confirming that the velocity and turbulence fields are well-settled.

It is important to note two limitations of this comparison. First, the `atmBoundaryLayerInletVelocity` boundary condition in OpenFOAM v10 implements a neutral logarithmic profile $U(z) = U_{\mathrm{ref}} \ln(z/z_0)/\ln(z_{\mathrm{ref}}/z_0)$ scaled to the prescribed $U_{\mathrm{ref}} = 7.7\,\mathrm{m\,s^{-1}}$; it does not accept an Obukhov length parameter and therefore does not impose the stability correction $\psi_m(z/L)$ that would steepen the profile under stable stratification. The inlet profile shape is thus identical to the neutral case, differing only in magnitude. Second, `simpleFoam` does not solve the energy equation and therefore does not model the buoyancy-driven suppression of vertical mixing that is the primary physical mechanism by which stable stratification affects wake recovery. Consequently, this comparison tests the Gaussian wake model's response to a uniformly lower freestream velocity with a neutral-shaped profile—not to a stability-modified velocity gradient—and not the stability correction factor $\psi_m = 0.6$. Furthermore, the standard k–ε turbulence model does not include buoyancy production and destruction terms ($G_b = -\beta g_i \overline{\theta' u_i'}$, $\partial\theta/\partial z_i$) in the turbulent kinetic energy transport equation, even with a thermally coupled solver, the turbulence closure would require modification (e.g., via the Boussinesq-modified k–ε model) to capture stability-dependent mixing rates within the wake. A genuine validation of ψ_m would therefore require a stability-corrected inlet (e.g., via a custom boundary condition implementing the full MOST profile with ψ_m) a thermally-coupled solver such as `buoyantSimpleFoam` with appropriate temperature boundary con-

division and Reynolds buoyancy and a modified turbulence closure with buoyancy source terms—all of which remain targets for future work.

Figure 8(a) shows the half-height normalized streamwise velocity field from the stable-inflow R4350 simulation on the fine mesh. The measured inflow velocity at half-height is $U_{1/2} = 7.7\,\mathrm{m/s}$, closely matching the target from the MOST profile. The fine mesh resolves the stable boundary layer substantially better than the coarse mesh, with less than 1.5% downstream variation across the domain length (compared to 10% on the coarse mesh). The wake structure exhibits a narrower and less pronounced deficit compared to the neutral case (fig. 6), consistent with the lower downstream velocity since the inlet profile is a neutral log-law scaled to $U_{1/2} = 7.7\,\mathrm{m/s}$, the velocity gradient at half-height is actually shallower than in the neutral case ($\partial U/\partial z \propto U_{1/2}$) so the wake differences arise primarily from the reduced inflow velocity rather than from a modified profile shape. The contour lines at $U_{1/2}/U_{\infty} = 0.70$, 0.80, 0.90, and 0.95 show the wake extending approximately 6D downstream before recovering to within 5% of the local freestream.

Figure 8(b) compares the lateral wake velocity profiles extracted from the stable R4350 simulation at $x/D = 1$, 7, and 10 against the Gaussian wake model predictions with the stable correction factor $\epsilon_0 = 0.6$. Both the R4350 and analytical profiles are normalized by the local freestream velocity at each downstream station (averaged over the field cells at $|y - y_{hub}| > 3D$). The RMSE between the analytical and R4350 profiles within $|y| < 2D$ decreases from 0.054 at $x/D = 1$ to 0.020 at $x/D = 10$, following the same decreasing trend observed in the neutral comparison (table 4). The Gaussian model again predicts deeper centerline deficits than the R4350 at all stations: the analytical centerline deficits are 31.6%, 25.4%, and 16.1% at $x/D = 1$, 7, and 10, compared to R4350 values of 17.6%, 14.3%, and 11.1%. The resulting centerline deficit errors of 14–46% are approximately comparable to the neutral case (19–46%, table 4). It must appear counterintuitive that the neutral deficit error at $x/D = 1$ (46%) exceeds the stable value (30%), given that stable conditions introduce additional physics, this arises because the normalized deficit ($\Delta U/U_{\infty}$) is more sensitive to small absolute velocity differences at the higher neutral freestream velocity ($8.0\,\mathrm{m/s}$ vs. $7.7\,\mathrm{m/s}$), and because the $k-\varepsilon$ overmixing is proportionally more severe under neutral conditions where the ambient turbulence is lower relative to the shear-generated TKE. The fine-mesh stable-inflow results represent a substantial improvement over the coarse-mesh comparison (which exhibited deficit errors of 207–450% due to a combination of numerical diffusion and a 10%

downstream acceleration artefact). The remaining discrepancy is attributable primarily to the $k-\varepsilon$ turbulent mixing characteristics, although the stable inlet profile has a shallower gradient than the neutral case (since k is a neutral log-law scaled to a lower $U_{*,s}$), the turbulence model's response to the extensive fetch asymmetrism still generates comparable levels of wake-region TKE. Both modelling approaches predict qualitatively consistent wake structures (Gaussian-like lateral profiles that narrow and deepen with increasing downstream distance), and the RMSE metric captures the integrated profile agreement. The stable-inflow RMSE values (0.049–0.054) are comparable to but slightly larger than the neutral-case values (0.043–0.049), with the difference attributable to the reduced wake signal-to-noise ratio at the lower stable wind speed and the inherent variability of the $k-\varepsilon$ closure under different downstream velocities.

The analytical RANS discrepancy under stable conditions (controlling deficit errors of 41–46%, table 4) is comparable to the neutral case (37–46%, table 4), indicating that the fast mode substantially reduces the previously observed stable-condition penalty. Nonetheless, the Gaussian model overpredicts wake deficits under stable inflow by a factor of approximately 1.4–1.8 relative to the RANS solution, and the cross-row power reductions reported in section 5.2 (e.g., 38% under stable conditions) may be accordingly overstated. Propagating the stable-condition RMSE (0.049–0.054) through the power calculation suggests an uncertainty in the stable-column farm power values (table 5) of approximately $\pm$ 11%. This estimate is obtained by applying the RMSE-derived velocity uncertainty ($\delta U/U \approx 2.5\%$) only to the wake-affected rows (Rows 2 and 3, which contribute six of nine turbines), since the front-row turbines operate in undisturbed flow and are unaffected by wake-model errors; the resulting per-turbine power uncertainty of approximately $3 \times (\delta U/U) \approx 8$ MW is therefore diluted by the unaffected front row when averaged over the full nine-turbine farm, yielding a farm-level uncertainty of $(6$ MW$)/(\approx 53$ MW$) \approx 11\%$. Two partially offsetting biases affect this estimate: the RMSE is normalised by the freestream velocity rather than the lower effective velocity at wake-affected rows, which underestimates the relative velocity uncertainty (normalising by the effective velocity would yield per-turbine uncertainties of approximately 48 MW rather than 8 MW), conversely, the linearised $P \propto U^3$ sensitivity overestimates the power perturbation for the finite velocity errors involved. These biases partially cancel, and the RMSE decreases with downstream distance (from 0.054 at $x/D = 3$ to 0.049 at $x/D = 10$), so the $\pm$ 11% farm-level range remains a reasonable

able order-of-magnitude estimate. This uncertainty is comparable to the 5% mesh-related uncertainty and does not affect the qualitative ranking of terrain stability combinations. The matched-velocity analysis (section 5.4), which accelerates approximately 5% of the total power variation to make inverters differences, may modestly overestimate the stability-driven wake component under stable conditions, although the dominant finding—that hub-height wind speed accounts for the vast majority of the stability effect—remains robust.

The fine mesh substantially reduces the developing boundary layer artifact observed on the coarse mesh, with freestream velocity variation of less than 1.5% over 8rD downstream (compared to 10% on the coarse mesh). This modest variation has negligible impact on the single-turbine comparison and confirms that the fine mesh resolution is sufficient to maintain a nearly uniform freestream across the wake analysis region. For future multi-turbine farm comparisons under stable inflow, where downstream rows at 5rD and 10rD may be more sensitive to residual boundary layer development, a longer inflow development region or recycled inflow conditions would provide additional assurance that the freestream profile is fully established.

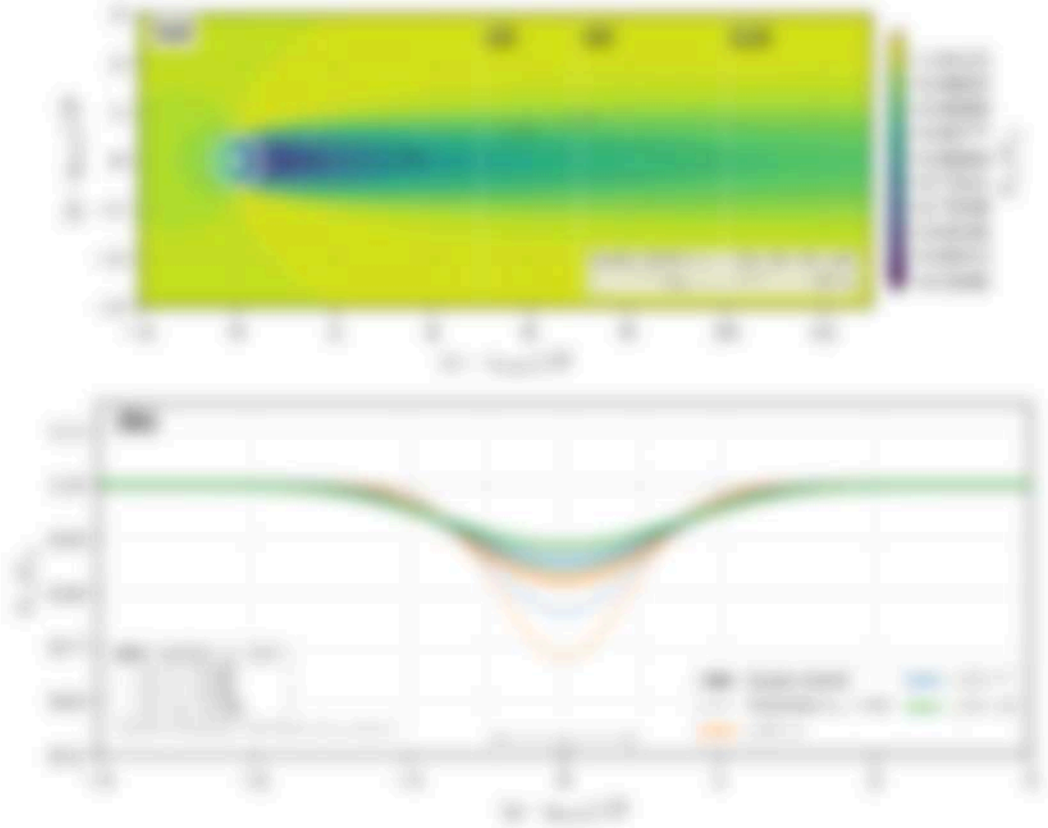

Figure 9: Comparison of RANS simulations and analytical Gaussian wake model for a single NREL 5 MW turbine: (a) wake-centerline velocity deficit $\Delta U_{wake}/U_\infty$ corresponding to stable ABL/RT conditions with $z_i = 1.0\,\mathrm{km}$, $z_i/L = 100$ and $z_i = 300\,\mathrm{m}$, $z_i/L = 30$ from OpenFOAM simpleFoam; $U_\infty = 8\,\mathrm{m\,s^{-1}}$, $H = 90\,\mathrm{m}$, $D = 126\,\mathrm{m}$, $TI_0 = 6\%$. (b) wake-area averaged hub-height normalized streamwise velocity from OpenFOAM simpleFoam; $U_\infty = 8\,\mathrm{m\,s^{-1}}$, $H = 90\,\mathrm{m}$, $D = 126\,\mathrm{m}$, $TI_0 = 6\%$. (c) wake-area averaged hub-height normalized streamwise velocity from OpenFOAM simpleFoam; $U_\infty = 8\,\mathrm{m\,s^{-1}}$, $H = 90\,\mathrm{m}$, $D = 126\,\mathrm{m}$, $TI_0 = 6\%$. (d) wake-area averaged hub-height normalized streamwise velocity from OpenFOAM simpleFoam; $U_\infty = 8\,\mathrm{m\,s^{-1}}$, $H = 90\,\mathrm{m}$, $D = 126\,\mathrm{m}$, $TI_0 = 6\%$. (e) wake-area averaged hub-height normalized streamwise velocity from OpenFOAM simpleFoam; $U_\infty = 8\,\mathrm{m\,s^{-1}}$, $H = 90\,\mathrm{m}$, $D = 126\,\mathrm{m}$, $TI_0 = 6\%$. (f) wake-area averaged hub-height normalized streamwise velocity from OpenFOAM simpleFoam; $U_\infty = 8\,\mathrm{m\,s^{-1}}$, $H = 90\,\mathrm{m}$, $D = 126\,\mathrm{m}$, $TI_0 = 6\%$. (g) wake-area averaged hub-height normalized streamwise velocity from OpenFOAM simpleFoam; $U_\infty = 8\,\mathrm{m\,s^{-1}}$, $H = 90\,\mathrm{m}$, $D = 126\,\mathrm{m}$, $TI_0 = 6\%$. (h) wake-area averaged hub-height normalized streamwise velocity from OpenFOAM simpleFoam; $U_\infty = 8\,\mathrm{m\,s^{-1}}$, $H = 90\,\mathrm{m}$, $D = 126\,\mathrm{m}$, $TI_0 = 6\%$. (i) wake-area averaged hub-height normalized streamwise velocity from OpenFOAM simpleFoam; $U_\infty = 8\,\mathrm{m\,s^{-1}}$, $H = 90\,\mathrm{m}$, $D = 126\,\mathrm{m}$, $TI_0 = 6\%$. (j) wake-area averaged hub-height normalized streamwise velocity from OpenFOAM simpleFoam; $U_\infty = 8\,\mathrm{m\,s^{-1}}$, $H = 90\,\mathrm{m}$, $D = 126\,\mathrm{m}$, $TI_0 = 6\%$. (k) wake-area averaged hub-height normalized streamwise velocity from OpenFOAM simpleFoam; $U_\infty = 8\,\mathrm{m\,s^{-1}}$, $H = 90\,\mathrm{m}$, $D = 126\,\mathrm{m}$, $TI_0 = 6\%$. (l) wake-area averaged hub-height normalized streamwise velocity from OpenFOAM simpleFoam; $U_\infty = 8\,\mathrm{m\,s^{-1}}$, $H = 90\,\mathrm{m}$, $D = 126\,\mathrm{m}$, $TI_0 = 6\%$. (m) wake-area averaged hub-height normalized streamwise velocity from OpenFOAM simpleFoam; $U_\infty = 8\,\mathrm{m\,s^{-1}}$, $H = 90\,\mathrm{m}$, $D = 126\,\mathrm{m}$, $TI_0 = 6\%$. (n) wake-area averaged hub-height normalized streamwise velocity from OpenFOAM simpleFoam; $U_\infty = 8\,\mathrm{m\,s^{-1}}$, $H = 90\,\mathrm{m}$, $D = 126\,\mathrm{m}$, $TI_0 = 6\%$. (o) wake-area averaged hub-height normalized streamwise velocity from OpenFOAM simpleFoam; $U_\infty = 8\,\mathrm{m\,s^{-1}}$, $H = 90\,\mathrm{m}$, $D = 126\,\mathrm{m}$, $TI_0 = 6\%$. (p) wake-area averaged hub-height normalized streamwise velocity from OpenFOAM simpleFoam; $U_\infty = 8\,\mathrm{m\,s^{-1}}$, $H = 90\,\mathrm{m}$, $D = 126\,\mathrm{m}$, $TI_0 = 6\%$. (q) wake-area averaged hub-height normalized streamwise velocity from OpenFOAM simpleFoam; $U_\infty = 8\,\mathrm{m\,s^{-1}}$, $H = 90\,\mathrm{m}$, $D = 126\,\mathrm{m}$, $TI_0 = 6\%$. (r) wake-area averaged hub-height normalized streamwise velocity from OpenFOAM simpleFoam; $U_\infty = 8\,\mathrm{m\,s^{-1}}$, $H = 90\,\mathrm{m}$, $D = 126\,\mathrm{m}$, $TI_0 = 6\%$. (s) wake-area averaged hub-height normalized streamwise velocity from OpenFOAM simpleFoam; $U_\infty = 8\,\mathrm{m\,s^{-1}}$, $H = 90\,\mathrm{m}$, $D = 126\,\mathrm{m}$, $TI_0 = 6\%$. (t) wake-area averaged hub-height normalized streamwise velocity from OpenFOAM simpleFoam; $U_\infty = 8\,\mathrm{m\,s^{-1}}$, $H = 90\,\mathrm{m}$, $D = 126\,\mathrm{m}$, $TI_0 = 6\%$. (u) wake-area averaged hub-height normalized streamwise velocity from OpenFOAM simpleFoam; $U_\infty = 8\,\mathrm{m\,s^{-1}}$, $H = 90\,\mathrm{m}$, $D = 126\,\mathrm{m}$, $TI_0 = 6\%$. (v) wake-area averaged hub-height normalized streamwise velocity from OpenFOAM simpleFoam; $U_\infty = 8\,\mathrm{m\,s^{-1}}$, $H = 90\,\mathrm{m}$, $D = 126\,\mathrm{m}$, $TI_0 = 6\%$. (w) wake-area averaged hub-height normalized streamwise velocity from OpenFOAM simpleFoam; $U_\infty = 8\,\mathrm{m\,s^{-1}}$, $H = 90\,\mathrm{m}$, $D = 126\,\mathrm{m}$, $TI_0 = 6\%$. (x) wake-area averaged hub-height normalized streamwise velocity from OpenFOAM simpleFoam; $U_\infty = 8\,\mathrm{m\,s^{-1}}$, $H = 90\,\mathrm{m}$, $D = 126\,\mathrm{m}$, $TI_0 = 6\%$. (y) wake-area averaged hub-height normalized streamwise velocity from OpenFOAM simpleFoam; $U_\infty = 8\,\mathrm{m\,s^{-1}}$, $H = 90\,\mathrm{m}$, $D = 126\,\mathrm{m}$, $TI_0 = 6\%$. (z) wake-area averaged hub-height normalized streamwise velocity from OpenFOAM simpleFoam; $U_\infty = 8\,\mathrm{m\,s^{-1}}$, $H = 90\,\mathrm{m}$, $D = 126\,\mathrm{m}$, $TI_0 = 6\%$.

3. Results and discussion

3.1. Terrain effects under neutral conditions

The effect of terrain complexity on wind farm performance is first examined under neutral atmospheric conditions, isolating the terrain influence from stability effects. Figure 10 presents hub-height velocity fields for all nine primary cases, computed using the Gaussian wake model with superposition. Under neutral conditions, the flat terrain case (C1) exhibits the classical pattern of elongated wake deficits behind each turbine row, with progressive deepening of the cumulative deficit at downstream rows. The hills terrain (C2) produces faster wake recovery due to the enhanced expansion rate ($\alpha_w = 1.25$), partially disrupting the regular deficit patterns. The mountainous terrain (C3) generates the fastest wake recovery ($\alpha_w = 1.5$), with wake deficits nearly dissipated between rows.

Figure [illegible]: Normalized hub-height velocity fields U/U_∞ for the 3×3 (asymmetric) matrix of terrain types (rows) and atmospheric stability conditions (columns). White circles indicate turbine rotor positions.

The velocity deficit fields at hub height are shown in Fig. 11 for flat and inversion-driven terrain under all three stability conditions. The deficit magnitude $\Delta U/U_\infty = 1 - U/U_\infty$ reveals the spatial extent and intensity of wake interactions, with labelled contour lines at $\Delta U/U_\infty = 0.05$, 0.10, 0.20, and 0.30 indicating key deficit thresholds. Under stable conditions, wake deficits remain deep (> 0.30) far downstream, while convective conditions produce rapid wake recovery with deficits falling below 0.10 within two rotor-row spacings. The ambient TKE from the MOST profiles (I_{amb}) is annotated in each panel to indicate the stability-dependent mixing environment. The analytical model does not resolve wake-generated turbulence; the deficit patterns arise from the stability-dependent effective wake expansion rate k_{eff} (eq. 11).

Figure 11: Rain-height velocity deficit fields $\Delta U/U_{\infty}$ for flat terrain (top row) and terrain-tailored terrain (bottom row) under z_0 of stable, N, and unstable conditions. Dashed circles indicate turbine rotor positions. Contour lines are identified at key deficit thresholds. The maximum Δ_{max} values indicate the sublimit 7000 from 36000 profiles for each stability condition, such that Δ_{max} is obtained across terrain types for a given stability, thus because the 36000 profiles aligned with an z_0, z_0 and Δ, not on the terrain correction factor z_0.

The centerline velocity deficit profiles Eq. 12 quantify the terrain effect on wake recovery. At $x/D = 10$ downstream of the front row, the wake deficit on flat terrain reaches 0.26, compared to 0.24 for hilly and 0.23 for terrain-tailored terrain. This 10% reduction in wake deficit from flat to accommodation terrain is attributable to the larger effective wake expansion rate k_{eff}, which accelerates the entrainment of high-momentum air from the wake periphery. However, the effect on total farm power is modest: accommodation terrain produces 46.21 MW versus 44.94 MW for flat terrain under neutral conditions, a difference of only 1.3% (table 5). The modest power increase despite the substantial wake deficit reduction arises because terrain-enhanced mixing affects only the wake-affected downstream rows, while the front row (operating

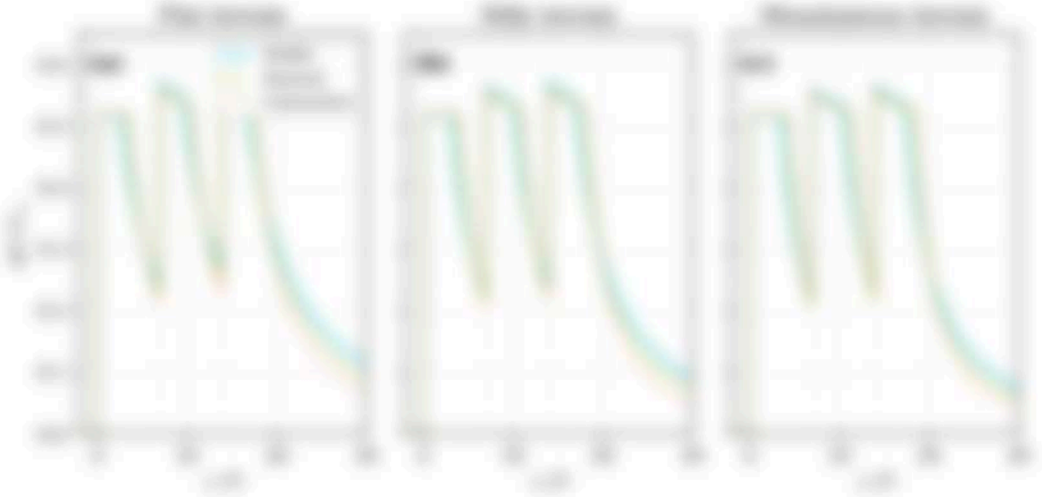

Figure 18: Cumulative wake velocity deficit $\Delta U/U_{z_r}$ as a function of downstream distance for (a) flat, (b) hilly, and (c) mountainous terrain under the three atmospheric stability conditions. Vertical dashed lines indicate turbine rotor positions.

in undisturbed flow) contributes approximately one-third of the total farm power and is unaffected by the terrain correction factor.

3.3. Stability effects on flat terrain

The influence of atmospheric stability on wake dynamics and farm power is examined on flat terrain, isolating stability from terrain effects. Figure 19 presents vertical profiles of the normalized streamwise velocity at $x/D = 3$, 7, and 10 downstream of the front-row middle turbine. These profiles are generated by applying a Gaussian vertical distribution to the hub-height wake deficit, consistent with the model assumption that the wake profile is self-similar in both the lateral and vertical directions.

Under stable stratification (C1), the effective wake expansion rate ($k_{e_y} + k_{e_z} = 0.5 + 0.007 \times 0.6 + 1.0 \times 0.035$) produces a narrow, deep wake that persists far downstream. The normalized velocity deficit at hub height ($z/z_r = 1$) remains 0.36 at $x/D = 10$, compared to 0.28 for neutral (C2) and 0.19 for convective (C3) conditions. It is important to note that the different stability classes also correspond to different hub-height wind speeds (7.7, 9.0, and 10.0 m/s, as listed in table 2), so the absolute power differences reflect the combined effects of freestream velocity and wake recovery rate.

Figure 10: Vertical profiles of normalized streamwise velocity at (a) $x_c = 0 \cdot H$, (b) $x_c = 5 \cdot H$, and (c) $x_c = 10 \cdot H$ in flat terrain under the three stability conditions. The grey-shaded region indicates the cross-dale extent.

The corresponding profiles for hilly and mountainous terrain are presented in figs. 11 and 12. The same stability-dependent trends persist across all terrain types, but with terrain-accelerated intensity. On hilly terrain (fig. 11), the increased terrain correction factor enhances wake recovery relative to the flat terrain case, reducing the hub-height deficit by approximately 10% for the stable condition. On mountainous terrain (fig. 12), the deficit reduction reaches 15–20% under stable conditions compared to flat terrain.

Eddy terrain

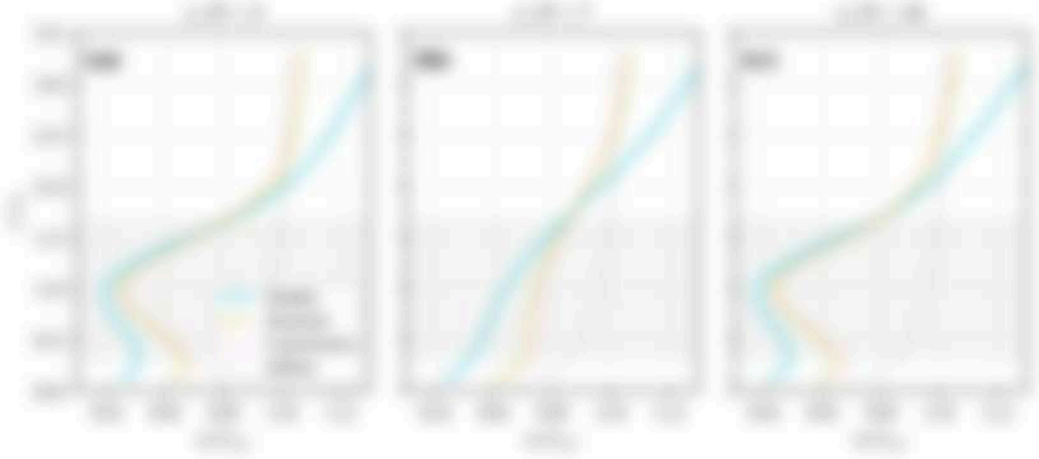

Figure 14. Vertical profiles of normalized streamwise velocity at (a) $x/R = 0$, (b) $x/R = 1$, and (c) $x/R = 10$ in eddy terrain under the three stability conditions.

Roughness terrain

Figure 15. Vertical profiles of normalized streamwise velocity at (a) $x/R = 0$, (b) $x/R = 1$, and (c) $x/R = 10$ in roughness terrain under the three stability conditions.

The row-by-row power analysis (fig. 16) reveals the cascade of wake losses through successive turbine rows. Under stable conditions, the front row produces 1.89 MW per turbine on average, while the third (rear) row produces only 0.66 MW—a reduction of 65%. Under neutral conditions, this reduction is 51% (from 2.00 to 1.21 MW), and under convective conditions it is 51% (from 2.06 to 1.77 MW). The dominant effect of stability on total farm power arises primarily from the different freestream wind speeds at hub height (7.1, 9.0, and 10.0 m s^{-1} for stable, neutral, and convective conditions, respectively) rather than from differences in wake recovery alone. Specifically, the front-row power ratio between convective and stable conditions is $(10.0/7.1)^3 \approx 2.8$, which accounts for the bulk of the observed power difference. The stable-sublist RANS comparison (section 4.3) indicates that the analytical model overpredicts centerline wake deficits relative to the RANS by a larger factor under stable conditions than under neutral conditions; consequently, the 60% rear-row reduction reported here carries an uncertainty of approximately 12–40% (see discussion at the end of section 4.3), though the qualitative trend of increasing wake losses with increasing stability is well established in the literature [14].

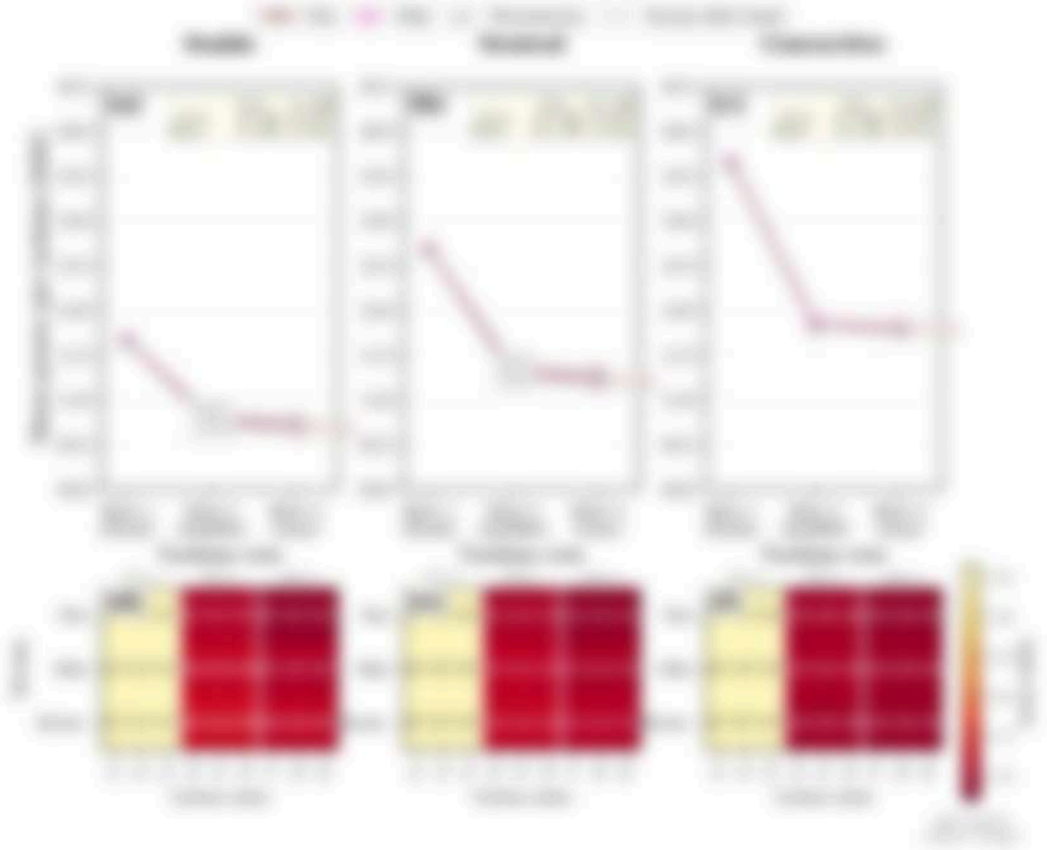

Figure 16. Mean hy-con points ± standby across vortex types for (a) stable, (b) neutral, and (c) convective conditions. Upper panels show connected-slope charts tracing the mean points per vortex from Row 1 (Vortex) through Row 3 (stable) to Row 4 (vortex) for each vortex type; shaded vortex-effect bands highlight the spread between flat and anisotropic vortex at each row. Individual vortex points are shown as semi-transparent context markers to indicate within-row variability. Anisotropy-index panels for the equidistant-from-4-row vortex lens for this vortex. Lower panels (d–f) present vortex-level vortex heatmaps for all nine vortices across the three vortex types, with row sequences and anisotropy points values (ANIX), each heatmap panel uses per-panel colour scaling to enhance within-condition contrast; the absolute points ranges differ between stability conditions. Small within-anisotropic vortex these points per vortex type.

An alternative view is provided in fig. 17, which separates the cost for cost points data by vacuum type. This representation makes clear that the availability-driven spread in determinism cost points has a far larger than the vacuum-driven spread.

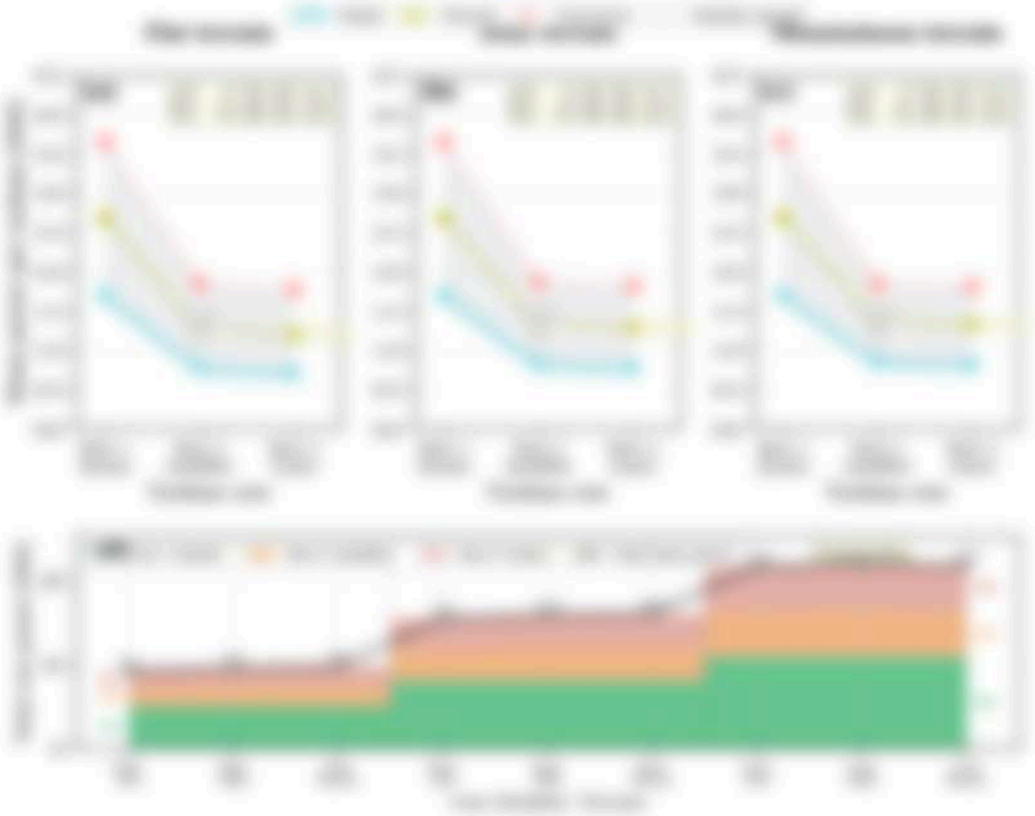
Fiber terrain
Small wetland
Mountainous terrain
Rural
Urban
Suburban
Fiber
Wireless
Hybrid
Fiber Access Network Cost ($/km)
Fiber Access Network Cost ($/km)
Fiber Access Network Cost ($/km)

3.3 Combined terrain–stability interaction

Figure 10 presents the wind farm power output for all nine primary cases as a heatmap across the terrain–stability parameter space. The dominant axis of variation is atmospheric stability: moving from stable to convective conditions increases farm power by a factor of 2.3–2.5 across all terrain types. The terrain effect is secondary, with mountainous terrain producing 2.4% more power than flat terrain for each stability class. Notably, this 2.4% terrain-induced power variation is comparable to or smaller than the model's own validation uncertainty (4–11% under stable conditions, as reported in section 3.0), indicating that the terrain effect cannot be reliably distinguished from the model's inherent uncertainty. The terrain–thermal pattern in fig. 10 appears as nearly uniform horizontal bands, reflecting this limited sensitivity. This is an important negative result: it suggests that the analytical correction-factor approach may lack the resolution to meaningfully differentiate terrain types, and that terrain-resolved CFD would be needed to quantify terrain effects with confidence.

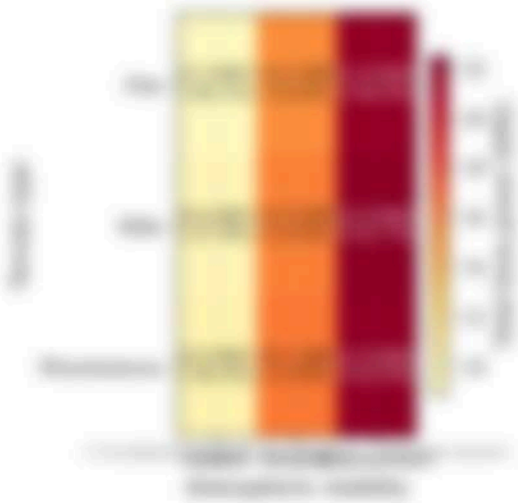

Figure 4: Total farm power output (kW) for the 3×3 parameter matrix of terrain state and stability conditions. Percentages indicate the change relative to the first scenario (cell 1,1).

Within the multiplicative correction framework (eq. 21), the terrain–stability interaction is inherently non-additive: the combined effect of terrain and stability is not the sum of their individual effects. Under stable conditions, the power increase from flat to mountainous terrain is 6.0% (from 9.24 to 9.97 MW), which is larger than the 3.9% increase observed under neutral conditions. This is because the terrain correction factor (c_{ij}) multiplies a smaller baseline expansion rate under stable conditions, so the relative increase in mixing intensity is proportionally more beneficial for wake recovery. Conversely, under convective conditions, the terrain effect diminishes to only 0.4% (from 21.83 to 21.91 MW), because the already-high effective expansion rate places the wake deficit in a regime of diminishing returns where further increasing C_{ij} has negligible effect on wake recovery. The hilly terrain (1%, 22.05 MW) actually produces slightly more power than mountainous terrain (1%, 21.91 MW) under convective conditions, a non-monotonic behaviour arising from the Gaussian deficit formula approaching zero at very high expansion rates. This effect is a mathematical property of the model rather than a physical prediction, and underscores the need for resolved CFD to investigate such interactions in detail.

An important caveat applies to the results presented in table 5 and fig. 10: the mast power values in the terrain–stability matrix depend directly on the

Table 1. Total burst power output (MW) for all nine primary cases and percentage change relative to the first nominal baseline (1.0). [a] Values in the Neutral column are validated against BATSE; values in the Stable and Convective columns depend on the unvalidated convection factors κ_c (see text).

		Atmospheric instability		
		Stable[a]	Neutral	Convective[a]
Solar wind	Fast	9.34 (-46.1%)	17.31 (baseline)	25.49 ($+46.5\%$)
	Slow	9.69 (-47.9%)	18.46 ($+6.6\%$)	26.68 ($+46.8\%$)[b]
	Stream interaction	9.97 (-46.1%)	18.71 ($+8.0\%$)	25.76 ($+48.8\%$)

[a] Power values computed from the analytical scale model with instability and terrain correction factors.

[b] Slow terrain (CS) produces slightly more power than mountainous terrain (CM) under convective conditions, a non-monotonic behaviour arising from the Gaussian deficit formula approaching zero at very high expansion rates (see text).

[c] Stable and convective results depend on the empirical correction factors $\kappa_c = 0.6$ and $\kappa_c = 1.8$, respectively, which are calibrated to qualitative GEO trends but have not been validated against buoyancy-coupled CFD or field data (section 4.8). Only the neutral column is directly validated against BATSE.

stability correction factors κ_c and the terrain correction factors κ_t, whose values are calibrated to qualitative GEO trends but have not been validated against buoyancy-coupled CFD or field data for any specific terrain stability combination (section 4.8). The BATSE comparison validates only the inflow profile response under stable conditions (using $\kappa_c = 0.6$, which does not model buoyancy), not the value of $\kappa_c = 0.6$ itself. Consequently, the parameter results should be interpreted as an exploration of the model's response to assumed correction factors, rather than as validated predictions. The sensitivity analysis (section 5.7) shows that varying κ_c for cMPI produces burst power changes of ± 5–9% under stable conditions, providing a quantitative measure of how sensitive the results are to the assumed values.

These model predictions have practical implications if the qualitative trends are confirmed by higher-fidelity simulations: in regions characterized by predominantly stable stratospheric conditions, terrain with moderate topographic complexity could yield a meaningful improvement in burst power

output by enhancing wake mixing. In contrast, for sites dominated by convective conditions, terrain complexity would provide negligible benefit to wake recovery.

3.4. Matched-velocity sensitivity analysis

To isolate the effect of stability on wake recovery from the confounding influences of different hub-height wind speeds, a matched-velocity sensitivity analysis is performed. The three stability conditions (stable, neutral, convective) are re-evaluated with the friction velocity u_* adjusted in each case to yield a common hub-height wind speed of $U_h = 9.0\,\mathrm{m\,s^{-1}}$ on flat terrain; all other atmospheric parameters (Obukhov length L, ABL height h, surface temperature, and temperature lapse rate) remain at their stability-specific values from table 2. This approach follows the methodology advocated by Du et al. [56] for properly controlled stability comparisons. Since eq. (8) is linear in u_* for a given L, the inversion is exact: $u_* = U_h\kappa / [\ln(z_h/z_0) - \psi_m(z_h/L)]$, with $\ln(90/0.03) = 8.006$. The adjusted friction velocities are: $u_* = 0.351\,\mathrm{m\,s^{-1}}$ in stable ($L = 200\,\mathrm{m}$, $\psi_m = -2.37$), $u_* = 0.450\,\mathrm{m\,s^{-1}}$ in neutral ($\psi_m = 0$), and $u_* = 0.486\,\mathrm{m\,s^{-1}}$ in convective ($L = -200\,\mathrm{m}$, $\psi_m = 0.73$). These values satisfy the MOST profile to within rounding; for example, $u_*^{(\mathrm{stable})} = 0.351 \times 0.4\,[\ln(z_h/z_0) - \psi_m] = 0.351 \times 8.006 - (-2.37) = 0.351 \times 10.376 = 9.00\,\mathrm{m\,s^{-1}}$. The stable case requires a lower u_* because the stable stability correction $\psi_m(z/L) = -5\,z/L$ is positive for $z/L > 0$ (stable), so that the full MOST argument $[\ln(z/z_0) - \psi_m]$ exceeds the neutral log-law value. Increasing the velocity for a given u_* physically, stable stratification suppresses vertical mixing and steepens the velocity gradient, so hub-height wind speed is higher relative to the surface friction velocity. Conversely, the convective correction ($\psi_m < 0$) reduces the effective log-law term, decreasing velocity for a given u_* because convective mixing flattens the velocity profile, requiring a higher u_* to achieve the same hub-height wind speed.

Figure 10 shows the resulting row-by-row power for the matched-velocity cases. With the freestream velocity equalized, the front-row power is identical across all three stability conditions (3.60 MW per turbine). The remaining differences arise exclusively from the stability-dependent wake expansion rate. The total farm power ranges from 12.91 MW (stable) to 13.21 MW (neutral) to 13.31 MW (convective), corresponding to a 3.0% variation between stable and neutral and a 3.7% variation between stable and convective conditions. This is substantially smaller than the factor-of-2.5 variation observed in the unmatched analysis (table 5), confirming that the vast majori-

ity of the 'mobility effect' in the primary parametric study is driven by the different hub-height wind speeds prescribed by MOST. The stable matched-velocity case produces less power than the neutral case despite the equal hub-height wind speed because the lower ABL height under stable conditions (300 m vs. 1000 m) causes a TKE decay at hub height (eq. (11)), reducing the ambient TI and hence the effective wake expansion rate. The combined effect of mobility on wake recovery — approximately 7% between stable and convective conditions when wind speed is held constant — is meaningful but secondary. A methodological subtlety warrants mention: adjusting z_i to match U_h also changes the ambient turbulence intensity, since TI depends on z_i through the TKE parameterization (eq. (10)). The matched-velocity stable case has a higher z_i (0.051 m vs. 0.04 m) than the original 0.08 m z_i, which increases TI and partially compensates for the z_i = 0.6 reduction in wake expansion rate. The TI–centerline variation therefore reflects the net effect of z_i differences and z_i -induced TI changes, which partially oppose each other, rather than the z_i effect in isolation. A truly clean decomposition ordering only z_i would require matching both U_h and TI, which is not possible within the MOST framework since both depend on z_i, L, and z_0. Nevertheless, the dominant finding — that hub-height wind speed accounts for the vast majority of the mobility-related power variation — is robust to this subtlety.

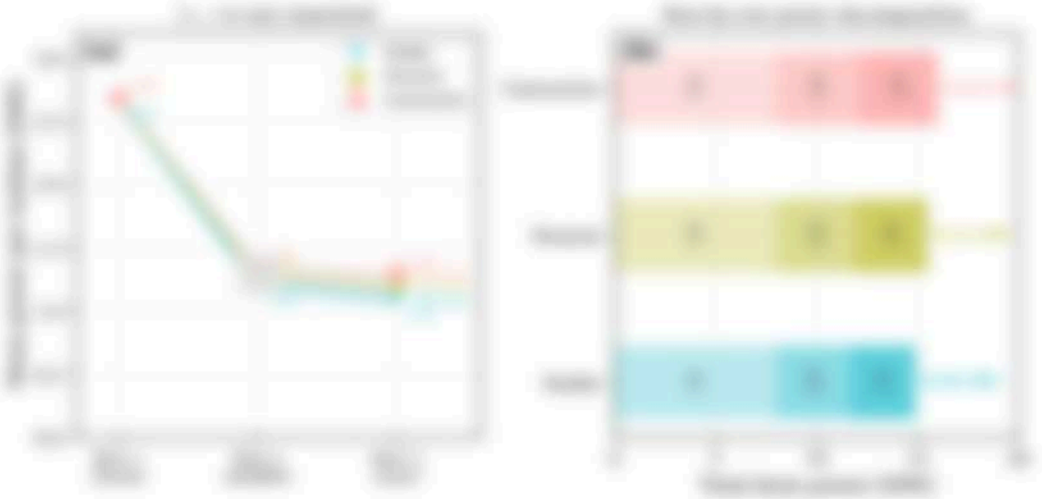

Figure 18: Hurdle-velocity sensitivity analysis at the terrain scale (τ_w = 0 mN m^{-2}) held constant across all farm stability conditions. (a) row-by-row mean power per turbine, showing directional front-row power and stability-dependent downstream differences. (b) row-by-row power decomposition showing the contributions of each turbine row to the total farm power.

3.3. Seasonal variation

The effect of seasonal atmospheric variation on farm power output is assessed using four hypothetical atmospheric profiles corresponding to winter, spring, summer, and autumn conditions, each with distinct friction velocity, Obukhov length, and ABL height. These profiles are constructed as 48-hr synthetic examples spanning the range of mid-latitude continental conditions reported in boundary-layer climatology studies [62]: winter (u_* = 0.35 m s^{-1}, L = 300 m, h = 400 m), spring (u_* = 0.45 m s^{-1}, L = −300 m, h = 800 m), summer (u_* = 0.30 m s^{-1}, L = −150 m, h = 1500 m), and autumn (u_* = 0.38 m s^{-1}, L = 500 m, h = 600 m). These values are not derived from a specific site's climatological record and should not be interpreted as predictions for any particular location; the purpose of this analysis is to demonstrate the sensitivity of farm power to seasonal variations in atmospheric parameters, not to quantify site-specific seasonal effects. Figure 20 shows the total farm power under each seasonal profile for flat and sinusoidal terrain.

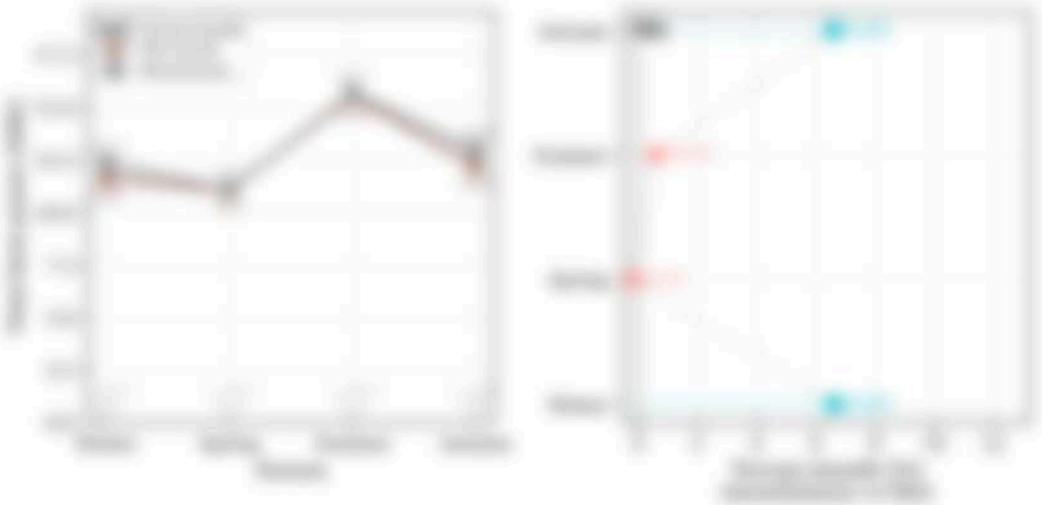

Figure 16. Seasonal variation in farm power. (a) wind farm power under four representative seasonal atmospheric profiles for fast and nonstationary terrain. (b) terrain-height percentage increase from flat to nonstationary for each season, reflecting the seasonally dependent magnitude of the terrain sensing effect.

Summer produces the highest farm power (15.6 MW for flat terrain) owing to the combination of a high friction velocity ($u_* = 0.30$ m s^{-1}) and convective conditions. Spring produces the lowest farm power (11.1 MW for flat terrain) despite its moderately high friction velocity ($u_* = 0.25$ m s^{-1}) because the weakly convective stability ($L = -300$ m) reduces the velocity profile via the positive ψ_m term in eq. (8), yielding a lower hub-height wind speed (7.9 m s^{-1} than winter (8.6 m s^{-1}). In contrast, winter's stable stratification ($L = 300$ m) causes the MOST profile as a negative ψ_m, which effectively increases hub-height wind speed for a given u_*. This explains the otherwise counterintuitive ordering in which winter ($u_* = 0.28$ m s^{-1}) produces higher farm power than spring ($u_* = 0.25$ m s^{-1}): the stability correction to the velocity profile more than offsets the lower friction velocity. The seasonal variation spans approximately 40% from the lowest to the highest seasonal case, illustrating that the combination of wind speed and stability distributions drives substantial AEP variability. The terrain effect is consistent across seasons, with nonstationary terrain providing up to 7% more power than flat terrain under stable seasonal conditions (winter), autumn) but negligible benefit under convective conditions. It should be noted that the 'seasonal variation' reported here is entirely driven by the choice of hypothetical MOST parame-

Figure 10. Power output change relative to dry air as a function of relative humidity for four ambient temperatures at standard atmospheric pressure.

state (κ_v, Fig. 2) for each season, which are illustrative rather than site-specific. the actual seasonal power variability at a given site would depend on the local climatological distributions of these parameters. The model does not simulate transient atmospheric processes such as diurnal cycling of instability or synoptic-scale weather variability.

3.6 Humidity sensitivity

The sensitivity of power output to humidity corrected on density (κ_ρ, 3.6.1) is evaluated as a post-processing correction. Figure 11 shows the power correction factor as a function of relative humidity for four ambient temperatures at standard pressure. The correction is negligible at cold temperatures (-0.1% at $0\,^\circ$C) but reaches -2.1% at $40\,^\circ$C and 80% RH. At the temperatures typical of the present study ($T = 298$–316 K), the humidity correction ranges from -0.01% to -0.17%, indicating that humidity corrections are relevant primarily for tropical and subtropical sites and can otherwise be neglected in the context of the other uncertainties inherent in the analytical wake modelling approach [18].

3.7 Sensitivity to empirical correction factors

The power predictions of the present model depend on the empirical stability correction factor κ_s and the terrain correction factor κ_t, whose values

were selected to reproduce qualitative trends from the GFD literature (see Sect. 2.2). To quantify the sensitivity of the results to these factors, a perturbation analysis is performed in which each factor is independently varied by $\pm 30\%$ from its nominal value while the other factor is held constant.

Figure 22(a) shows the resulting change in total farm power for an expansive-convective case spanning the terrain–stability parameter space. The sensitivity is asymmetric, with power decreasing more when the convection factors are reduced (narrower wakes, deeper deficit at downstream rotor) than it increases when the factors are enlarged (wider wakes). Under stable conditions driven on flat terrain—where the baseline C_{2p} is smallest and wake deficits are deepest—a $\pm 30\%$ change in either α_c or β_c produces a -3.1% to $+2.0\%$ change in total farm power. Under convective conditions on mountainous terrain—where C_{2p} is already large and wakes are nearly dissipated between rotors—the same perturbation produces a $+0.5\%$ to -1.2% change, reflecting the diminishing-returns regime.

Within the multiplicative structure of eq. (5), the stability and terrain correction factors are interchangeable in terms of their effect on C_{2p}: a 30% increase in α_c has the same effect as a 30% increase in α_t. This is because the effective expansion rate depends only on the product $\alpha_c \alpha_t$, not on the individual values. The sensitivity to each factor is therefore identical (Eq. 25c), confirming that the model cannot independently discriminate between stability-driven and terrain-driven changes in turbulent mixing; it responds only to the net mixing intensity. This is a structural limitation of the multiplicative correction approach and would not hold in resolved CFD simulations, where stability and terrain modify the flow through physically distinct mechanisms.

Figure 22(b) presents the combined sensitivity as a contour map of total farm power across the α_c, α_t parameter space for the stable-unconstrained case (C7). The iso-power contours are approximately hyperbolic, reflecting the product dependence $C_{2p} \propto \alpha_c \alpha_t$. Power varies from 6.2 MW at the low corner ($\alpha_c = 0.3$, $\alpha_t = 0.8$) to 10.1 MW at the high corner ($\alpha_c = 0.9$, $\alpha_t = 2.0$), a range of 25% about the nominal value. The dashed rectangle indicates the $\pm 30\%$ range around the nominal operating point ($\alpha_c = 0.9$, $\alpha_t = 1.5$). Within this rectangle, the power variation is approximately $\pm 7\%$, indicating that the paper's principal conclusions regarding the relative importance of stability versus terrain are robust to moderate uncertainty in the empirical correction factors.

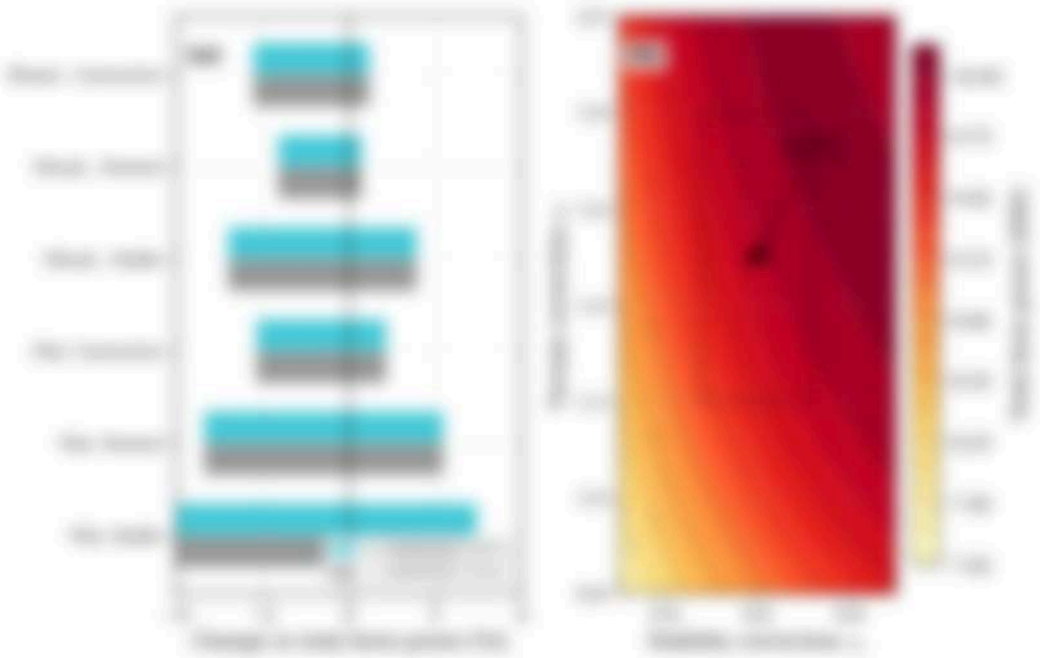

Figure 20: Sensitivity of wind farm power to the regional correction factors. (a) change in farm power for ±20% perturbations of the stability correction c_s and rotation correction c_r across the representative states. (b) contour map of wind farm power as a function of c_s and c_r for the stable-neutral-shear case (C1), with the star marking the nominal values and the dashed rectangle indicating the ±20% perturbation range.

6. Conclusions

This study has presented a systematic parametric assessment of wind farm performance under the combined effects of terrain complexity and atmospheric stability, using the Bastankhah and Porté-Agel 2D Gaussian wake model with stability and terrain correction factors applied to the Fuschlsee and Porté-Agel [12] turbulence intensity-dependent wake expansion rate. The principal findings are as follows.

The combination of hub-height wind-speed differences and stability-dependent wake recovery produces a 2.3-fold variation in wind farm power between stable and convective conditions. A substantial fraction of this variation arises from the different hub-height wind speeds associated with each stability class (7.7, 9.0, and 10.0 m s^{-1} for stable, neutral, and convective, respectively), since power scales with the cube of wind speed. When hub-height wind speed is held constant in a matched-velocity analysis, the residual wake-recovery

driven variation is approximately 7%, confirming that mobility affects wake dynamics meaningfully but that the dominant contributor to power differences across mobility classes in the SR3052 framework is the prescribed rotor velocity.

Terrain complexity exerts a secondary influence on farm power, with nonstationary terrain producing 2–4% more power than flat terrain through enhanced wake mixing, as captured by the terrain correction factor. This effect is most pronounced under stable stratification conditions, where the baseline wake expansion rate is low and the proportional benefit of additional mixing is greatest.

Within the multiplicative correction framework, the terrain mobility interaction is inherently non-additive. Under convective conditions, the high effective expansion rate places the model in a regime of diminishing returns where additional terrain mixing has negligible effect. This non-additivity is a structural property of the model, whether it accurately represents the physical terrain–mobility interaction requires verification through resolved CFD or LiDAR measurements.

Seasonal stratification variation produces a 40% swing in farm power between the lowest and highest representative profiles, driven primarily by the different friction velocities prescribed for each season. Humidity corrections to air density reduce power estimates by up to 2.1% at extreme conditions (30 °C, 80% RH), a correction relevant primarily for tropical and subtropical sites.

The analytical modelling approach adopted here has significant limitations that should guide interpretation of the results. The Gaussian wake model assumes self-similar wake profiles and does not resolve the detailed flow physics captured by RANS or LES, including terrain-induced flow separation and recirculation, low-level jets, wake meandering, Coriolis-driven wake deflection [18], interaction between thermal convective cells and wake structures, and changes in ABL height affecting wake recovery. The mobility and terrain correction factors are empirical and their values are uncertain, in particular, the terrain factors do not account for the specific orientation, slope, and roughness characteristics of real topography. The SR3052 derived turbulence intensity at hub height exhibits a counterintuitive mobility ordering (highest under stable conditions) due to the amplification of TKE by the z_{ref} function at heights that may exceed the surface layer depth, the mobility correction factors compensate for this artefact to produce physically reasonable effective wake expansion rates, but a more rigorous hub-height TI

parameterization would improve the model's physical basis. The wake superposition method is approximate and does not capture blockage effects [46] or deep-array wake phenomena [47]. Coriolis effects are neglected, which may influence wake deflection at the scales considered here. The SOWFA-based yaw-misalignment steady-state conditions and do not capture the transient evolution of the AMR during thermal or synoptic transitions, as modelled by Xiao et al. [48].

Comparisons against RANS simulations (OpenFOAM, $\lambda = $ actuator-disk) demonstrate consistency between the analytical and numerical frameworks. For a single turbine under neutral conditions on the fine mesh (766k cells, $\Delta x/D \approx 1.25$), the RMSE of the normalized lateral velocity profile decreases from 0.050 at $x/D = 1$ to 0.024 at $x/D = 10$, with the Gaussian model predicting deeper centerline deficits than the RANS (e.g., 0.471 vs. 0.674 at $x/D = 5$), consistent with the known overprediction of turbulent mixing by the standard $k-\varepsilon$ model [5]. Under stable inflow conditions on the same fine mesh, the RMSE values are 0.054, 0.046, and 0.049 at $x/D = 5$, 7, and 10, respectively, comparable to the neutral case and substantially improved relative to the coarse mesh; the comparison validates only the inflow profile response and not the buoyancy-driven wake suppression that would require a thermally-coupled solver. For the full 3×3 wind farm, the analytical model predicts a total farm power 1.3% higher than the RANS simulation (11.15 vs. 11.01 MW), with row-level differences of $+12\%$, -7%, and $+5\%$ for the front, middle, and rear rows, respectively. Extending this comparison to finer meshes and thermally-stratified simulations (e.g., [redacted]) to validate the stability correction factor κ_s remains a priority for future work. Propagating the RANS analytical velocity discrepancies through the cubic power relationship yields estimated farm-level power uncertainties of approximately 4–11% under stable conditions and 12–30% under neutral conditions; these estimates are conservative, as they apply the worst-case single-turbine RMSE uniformly to all wake-affected rows, and do not alter the qualitative ranking of terrain stability combinations reported in section 5.

It is worth noting how the present parametric framework relates to existing open-source tools. FLORIS [49] and FLOWERS [50] both implement the Gaussian wake model and support tunable wake expansion rates, while higher-fidelity tools such as SOWFA [51] provide LES-level resolution. The primary contribution of the present work is not the model itself but rather the systematic parametric analysis with SOWFA-coupled inflow profiles, the multi-lightcurve stability terrain correction framework, and the matched-velocity

methodology that separates wind-speed effects from wake-recovery effects. The matched-velocity analysis in particular is not a standard output of FLORIS or FLOWER, and the explicit characterization of how correction factors interact non-additively provides insight that goes beyond running individual cases. Nonetheless, reproducing the present parametric study within FLORIS would be straightforward and is encouraged as an independent verification.

Despite these limitations, the analytical framework provides a rapid and transparent means of identifying the dominant sensitivities in the terrain–mobility parameter space. The key practical insight is that terrain complexity has a much smaller effect on wind farm power than atmospheric stability conditions, and that the mobility effect is itself dominated by the downstream wind speed rather than the wake recovery rate. These findings can guide the prioritization of modelling effort in wind resource assessment: accurately characterizing the site wind climate (speed distributions and stability statistics) is more important for AEP prediction than detailed terrain resolved flow modelling, although the latter remains essential for understanding local loading, turbulence, and extreme conditions. Future work should validate the empirical correction factors against resolved RANS or LES simulations for specific terrain–mobility combinations, extend the parametric framework to include wake steering and yaw control strategies [35], and develop physically-based (rather than empirical) corrections for terrain and mobility effects within the analytical wake modelling framework.

CRediT authorship contribution statement

First Author: Conceptualization, Methodology, Software, Formal analysis, Investigation, Writing – original draft, Visualization. **Second Author**: Supervision, Writing – review & editing.

Declaration of competing interest

The authors declare that they have no known competing financial interests or personal relationships that could have appeared to influence the work reported in this paper.

Data availability

The Python scripts implementing the analytical wake model, atmospheric profile calculations, and figure generation, along with the OpenFOAM case files for the ALM/ADM actuator-disk simulations, will be deposited in a publicly accessible repository upon acceptance of this manuscript.

Acknowledgements

The authors gratefully acknowledge the use of computational resources provided by the Oxford Advanced Research Computing facility.

References

[1] F. Porté-Agel, M. Bastankhah, S. Shamsoddin, Wind-turbine and wind-farm flows: A review, Boundary-Layer Meteorology 174 (2020) 1–59. doi:10.1007/s10546-019-00473-0.

[2] R. J. A. M. Stevens, C. Meneveau, Flow structure and turbulence in wind farms, Annual Review of Fluid Mechanics 49 (2017) 311–339. doi:10.1146/annurev-fluid-010816-060206.

[3] R. Sanderse, S. P. van der Pijl, B. Koren, Review of computational fluid dynamics for wind turbine wake aerodynamics, Wind Energy 14 (7) (2011) 799–819. doi:10.1002/we.458.

[4] L. J. Vermeer, J. N. Sørensen, A. Crespo, Wind turbine wake aerodynamics, Progress in Aerospace Sciences 39 (6-7) (2003) 467–510. doi:10.1016/S0376-0421(03)00078-2.

[5] M. Calaf, C. Meneveau, J. Meyers, Large eddy simulation study of fully developed wind-turbine array boundary layers, Physics of Fluids 22 (2010) 015110. doi:10.1063/1.3291077.

[6] C. Meneveau, Big wind power: seven questions for turbulence research, Journal of Turbulence 20 (1) (2019) 2–20. doi:10.1080/14685248.2019.1584664.

[7] S. Ivanell, Actuator-Disk Models for Wind Turbine and Wind Farm Simulations, Ph.D. thesis, Royal Institute of Technology, Stockholm, Sweden (2009).

[8] M. Bastankhah, F. Porté-Agel, A new analytical model for wind-turbine wakes, Renewable Energy 70 (2014) 116–123. doi:10.1016/j.renene.2014.01.002.

[9] M. Bastankhah, F. Porté-Agel, Experimental and theoretical study of wind turbine wakes in yawed conditions, Journal of Fluid Mechanics 806 (2016) 506–541. doi:10.1017/jfm.2016.686.

[10] T. Ishihara, G.-W. Qian, A new Gaussian-based analytical wake model for wind turbines considering ambient turbulence intensities and thrust coefficient effects, Journal of Wind Engineering and Industrial Aerodynamics 177 (2018) 275–292. doi:10.1016/j.jweia.2018.04.010.

[11] A. Vasellas, F. Porté-Agel, Analytical modelling of wind farms: A new approach for power prediction, Energies 9 (8) (2016) 741. doi:10.3390/en9090741.

[12] S. Wharton, J. K. Lundquist, Assessing atmospheric stability and its impacts on rotor-disk wind characteristics at an onshore wind farm, Wind Energy 15 (4) (2012) 525–546. doi:10.1002/we.483.

[13] K. S. Hansen, R. J. Barthelmie, L. E. Jensen, A. Sommer, The impact of turbulence intensity and atmospheric stability on power deficits due to wind turbine wakes at Horns Rev wind farm, Wind Energy 15 (1) (2012) 183–196. doi:10.1002/we.512.

[14] M. Abkar, F. Porté-Agel, Influence of atmospheric stability on wind-turbine wakes: A large-eddy simulation study, Physics of Fluids 27 (2015) 035104. doi:10.1063/1.4913695.

[15] B. Lu, F. Porté-Agel, Large-eddy simulation of a very large wind farm in a stable atmospheric boundary layer, Physics of Fluids 23 (2011) 065101. doi:10.1063/1.3589857.

[16] B. Du, M. Ge, C. Zeng, et al., Effects of atmospheric stability on the recovery of wind-turbine wakes, Renewable Energy 174 (2021) 909–916. doi:10.1016/j.renene.2021.04.096.

[17] S. Xie, C. L. Archer, Self-similarity and turbulence characteristics of wind turbine wakes via large-eddy simulation, Wind Energy 20 (8) (2017) 1465–1477. doi:10.1002/we.2046.

[24] K. A. Kirk, H. F. Rowland, Unraveling the effects of atmospheric density on wakes with a controlled synthetic inflow methodology, arXiv preprint arXiv:2512.04145 (2025).

[25] S. Xiao, X. Zhu, G. Vasaikaban, D. F. Gayme, C. Meneveau, Wind farm dynamics over a diurnal cycle: Synthesis of a comprehensive large eddy simulation, web-services accessible dataset, arXiv preprint arXiv:2510.05885 (2025).

[26] S. Frandsen, A simple analytical wind park model considering atmospheric stability, Wind Energy 13 (1) (2010) 459–469. doi:10.1002/we.367.

[27] N. O. Jensen, A note on wind generator interaction, Risø National Laboratory (Risø-M-2411) (1983) 1–16.

[28] A. Peña, O. Rathmann, Atmospheric stability-dependent infinite wind-farm models and the wake-decay coefficient, Wind Energy 17 (5) (2014) 1269–1285. doi:10.1002/we.1628.

[29] Various, Review of OpenFOAM applications in the computational wind engineering: from wind environment to wind structural engineering, Mercuratus (2024). doi:10.1007/s43503-024-00008-w.

[30] L. P. Chamorro, F. Porté-Agel, A wind-tunnel investigation of wind-turbine wakes: boundary-layer turbulence effects, Boundary-Layer Meteorology 132 (2009) 129–149. doi:10.1007/s10546-009-9380-8.

[31] L. P. Chamorro, F. Porté-Agel, Effects of thermal stability and incoming boundary-layer flow characteristics on wind-turbine wakes: a wind-tunnel study, Boundary-Layer Meteorology 136 (2010) 515–533. doi:10.1007/s10546-010-9528-1.

[32] B. Yan, et al., A hierarchical nano-micro-scale coupled method for wind resource assessment over complex terrain, Wind Engineering (2025). doi:10.1177/[illegible].

[33] A. S. Wise, B. Solvsteldin, S. Vasiljevic, et al., Wind turbine wakes over a mountain ridge – a mesoscale microscale study, Journal of Physics: Conference Series (2265) (2022) 032016. doi:10.1088/1742-6596/2265/3/032016.

[20] J. Wang, Y. Ye, K. Zhang, J. Shen, Y. Cao, D. Zhou, An optimization framework for wind farm layout design using CFD-based Kriging model, Ocean Engineering 269 (2023) 113619. doi:10.1016/j.oceaneng.2022.113619.

[28] J. Kuitel, J. Bugajevsg, S. O. Ivanova, A simple model for cluster efficiency, European Wind Energy Association Conference and Exhibition (1986) 407–410.

[29] A. Stide, S. Lazare, Multi-fidelity Bayesian optimization of wind farm wake steering using wake models and large-eddy simulations, Proc. Torchlesses and Combinations (2024). doi:10.1007/s10696-024-09810-4.

[21] S. Eshkevizan-Rostami, A. Izadifar, M. Abbas, Data-driven fluid mechanics of wind farms: A review, Journal of Renewable and Sustainable Energy 14 (2) (2022) 022703. doi:10.1063/5.0084380.

[22] S. Bougouldia, F. Cruz, A. Wynn, S. Lazare, L. Magni, Data-driven optimization of wind farm layout and wake steering with large-eddy simulations, Wind Energy Science 9 (2024) 869–882. doi:10.5194/wes-9-869-2024.

[23] National Renewable Energy Laboratory, FLORIS Floris Redirection and Induction in Steady-state, https://github.com/NREL/Floris, version 4.0 (2024).

[24] M. M. Pedersen, P. van der Laan, M. Friis-Møller, J. Rinker, G. C. Larsen, PyWake — an open-source wind farm simulation tool, Journal of Physics: Conference Series 1256 (2019) 012035. doi:10.1088/1742-6596/1256/1/012035.

[25] S. Stipa, E. Ajuria Illarramendi, J. Brodzet, B. Thevenin, M. Bauerfeind, A. Meyers-Martin, FAST.X — an open-source, flutter-to-future, large-eddy simulation (LES) environment for wind farm flows, Wind Energy Science 9 (2024) 207–229. doi:10.5194/wes-9-207-2024.

[26] F. B. S. Lissaman, Energy effectiveness of arbitrary arrays of wind turbines, Journal of Energy 3 (6) (1979) 323–328. doi:10.2514/3.62441.

[37] J. Jonkman, S. Butterfield, W. Musial, G. Scott, Definition of a 5-MW reference wind turbine for offshore system development, Tech. Rep. NREL/TP-500-38060, National Renewable Energy Laboratory (2009).

[38] A. S. Monin, A. M. Obukhov, Basic laws of turbulent mixing in the surface layer of the atmosphere, Trudy Geofizicheskogo Instituta Akademiya Nauk SSSR 24 (151) (1954) 163–187.

[39] J. A. Businger, J. C. Wyngaard, Y. Izumi, E. F. Bradley, Flux-profile relationships in the atmospheric surface layer, Journal of the Atmospheric Sciences 28 (2) (1971) 181–189. doi:10.1175/1520-0469(1971)028<0181:FPRITA>2.0.CO;2.

[40] C. A. Paulson, The mathematical representation of wind speed and temperature profiles in the unstable atmospheric surface layer, Journal of Applied Meteorology 9 (6) (1970) 857–861. doi:10.1175/1520-0450(1970)009<0857:TMROWS>2.0.CO;2.

[41] R. B. Stull, An Introduction to Boundary Layer Meteorology, Kluwer Academic Publishers, Dordrecht, 1988.

[42] A. L. Buck, New equations for computing vapor pressure and enhancement factor, Journal of Applied Meteorology and Climatology 20 (12) (1981) 1527–1532. doi:10.1175/1520-0450(1981)020<1527:NEFCVP>2.0.CO;2.

[43] B. J. Barthelmie, K. Hansen, S. T. Frandsen, O. Rathmann, J. G. Schepers, W. Schlez, J. Phillips, K. Rados, A. Zervos, E. S. Politis, P. K. Chaviaropoulos, Modelling and measuring flow and wind turbine wakes in large wind farms offshore, Wind Energy 12 (5) (2009) 431–444. doi:10.1002/we.348.

[44] B. J. Barthelmie, S. C. Pryor, S. T. Frandsen, K. S. Hansen, J. G. Schepers, K. Rados, W. Schlez, A. Neubert, L. E. Jensen, S. Neckelmann, Quantifying the impact of wind turbine wakes on power output at offshore wind farms, Journal of Atmospheric and Oceanic Technology 27 (8) (2010) 1302–1317. doi:10.1175/2010JTECHA1398.1.

[45] A. Clarke, et al., On the quantification of air density corrections for offshore wind energy, Sustainability 11 (5) (2019) 1369. doi:10.3390/su11051369.

[46] S. Lazarides, I. Moreno. A parametric large-eddy simulation study of wind-farm blockage and gravity waves in conventionally neutral boundary layers. Journal of Fluid Mechanics 979 (2024) A14. doi:10.1017/jfm.2023.1088.

[47] S. Frandsen, R. Barthelmie, S. Pryor, O. Rathmann, S. Larsen, J. Højstrup, M. Thøgersen. Analytical modelling of wind speed deficit in large offshore wind farms. Wind Energy 9 (1-2) (2006) 39–53. doi:10.1002/we.189.